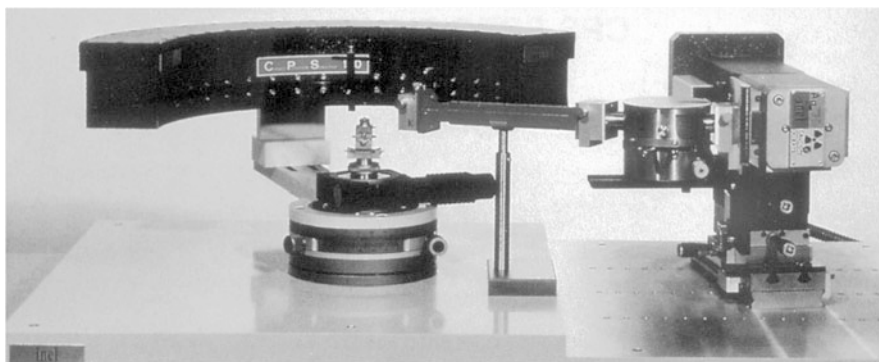


Chapter 1

Diffraction and the X-Ray Powder Diffractometer



1.1 Diffraction

1.1.1 Introduction to Diffraction

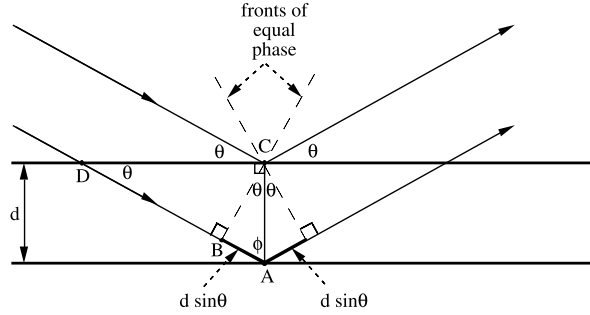
Materials are made of atoms. Knowledge of how atoms are arranged into crystal structures and microstructures is the foundation on which we build our understanding of the synthesis, structure and properties of materials. There are many techniques for measuring chemical compositions of materials, and methods based on inner-shell electron spectroscopies are covered in this book. The larger emphasis of the book is on measuring spatial arrangements of atoms in the range from 10^{-8} to 10^{-4} cm, bridging from the unit cell of the crystal to the microstructure of the material. There are many different methods for measuring structure across this wide range of distances, but the more powerful experimental techniques involve diffraction. To date, most of our knowledge about the spatial arrangements of atoms in materials has been gained from diffraction experiments. In a diffraction experiment, an incident wave is directed into a material and a detector is typically moved about to record the directions and intensities of the outgoing diffracted waves.

“Coherent scattering” preserves the precision of wave periodicity. Constructive or destructive interference then occurs along different directions as scattered waves are emitted by atoms of different types and positions. There is a profound geometrical relationship between the directions of waves that interfere constructively, which comprise the “diffraction pattern,” and the crystal structure of the material. The diffraction pattern is a spectrum of real space periodicities in a material.¹ Atomic periodicities with long repeat distances cause diffraction at small angles, while short repeat distances (as from small interplanar spacings) cause diffraction at high angles. It is not hard to appreciate that diffraction experiments are useful for determining the crystal structures of materials. Much more information about a material is contained in its diffraction pattern, however. Crystals with precise periodicities over long distances have sharp and clear diffraction peaks. Crystals with defects (such as impurities, dislocations, planar faults, internal strains, or small precipitates) are less precisely periodic in their atomic arrangements, but they still have distinct diffraction peaks. Their diffraction peaks are broadened, distorted, and weakened, however, and “diffraction lineshape analysis” is an important method for studying crystal defects. Diffraction experiments are also used to study the structure of amorphous materials, even though their diffraction patterns lack sharp diffraction peaks.

In a diffraction experiment, the incident waves must have wavelengths comparable to the spacings between atoms. Three types of waves have proved useful for these experiments. X-ray diffraction (XRD), conceived by von Laue and the Braggs, was the first. The oscillating electric field of an incident x-ray moves the atomic electrons and their accelerations generate an outgoing wave. In electron diffraction, originating with Davisson and Germer, the charge of the incident electron interacts with the positively-charged core of the atom, generating an outgoing electron wavefunction. In neutron diffraction, pioneered by Shull, the incident neutron wavefunction interacts with nuclei or unpaired electron spins. These three diffraction processes involve very different physical mechanisms, so they often provide complementary information about atomic arrangements in materials. Nobel prizes in physics (1914, 1915, 1937, 1994) attest to their importance. As much as possible, we will emphasize the similarities of these three diffraction methods, with the first similarity being Bragg’s law.

¹Precisely and concisely, the diffraction pattern measures the Fourier transform of an autocorrelation function of the scattering factor distribution. The previous sentence is explained with care in Chap. 10. More qualitatively, the crystal can be likened to music, and the diffraction pattern to its frequency spectrum. This analogy illustrates another point. Given only the amplitudes of the different musical frequencies, it is impossible to reconstruct the music because the timing or “phase” information is lost. Likewise, the diffraction pattern alone may be insufficient to reconstruct all details of atom arrangements in a material.

Fig. 1.1 Geometry for interference of a wave scattered from two planes separated by a spacing, d . The *dashed lines* are parallel to the crests or troughs of the incident and diffracted wavefronts. The important path length difference for the two rays is the sum of the two dark segments



1.1.2 Bragg's Law

Figure 1.1 is the construction needed to derive Bragg's law. The angle of incidence of the two parallel rays is θ . You can prove that the small angle in the little triangle is equal to θ by showing that the two right triangles, ABC and ACD, are similar. (*Hint: Look at the shared angle of $\phi = \frac{\pi}{2} - \theta$.*)

The interplanar spacing, d , sets the difference in path length for the ray scattered from the top plane and the ray scattered from the bottom plane. Figure 1.1 shows that this difference in path lengths is $2d \sin \theta$. Constructive wave interference (and hence strong diffraction) occurs when the difference in path length for the top and bottom rays is equal to one wavelength, λ :

$$2d \sin \theta = \lambda. \quad (1.1)$$

The right hand side is sometimes multiplied by an integer, n , since this condition also provides constructive interference. Our convention, however, sets $n = 1$. When there is a path length difference of $n\lambda$ between adjacent planes, we change d (even though this new d may not correspond to a real interatomic distance). For example, when our diffracting planes are (100) cube faces, and

$$2d_{100} \sin \theta = 2\lambda, \quad (1.2)$$

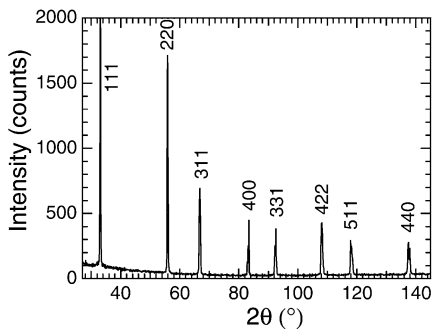
then we speak of a (200) diffraction from planes separated by $d_{200} = (d_{100})/2$.

A diffraction pattern from a material typically contains many distinct peaks, each corresponding to a different interplanar spacing, d . For cubic crystals with lattice parameter a_0 , the interplanar spacings, d_{hkl} , of planes labeled by Miller indices (hkl) are:

$$d_{hkl} = \frac{a_0}{\sqrt{h^2 + k^2 + l^2}}, \quad (1.3)$$

(as can be proved by the definition of Miller indices and the 3D Pythagorean theorem). From Bragg's law (1.1) we find that the (hkl) diffraction peak occurs at the

Fig. 1.2 Indexed powder diffraction pattern from polycrystalline silicon, obtained with Co $K\alpha$ radiation



measured angle $2\theta_{hkl}$:

$$2\theta_{hkl} = 2 \arcsin \left(\frac{\lambda \sqrt{h^2 + k^2 + l^2}}{2a_0} \right). \quad (1.4)$$

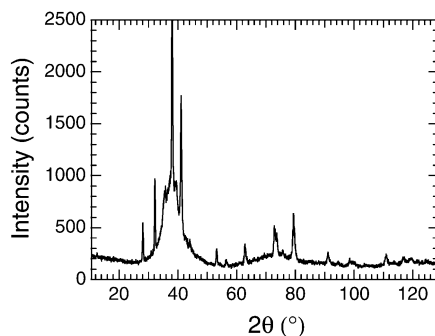
There are often many individual crystals of random orientation in the sample, so all possible Bragg diffractions can be observed in the “powder pattern.” There is a convention for labeling, or “indexing,” the different Bragg peaks in a powder diffraction pattern² using the numbers (hkl) . An example of an indexed diffraction pattern is shown in Fig. 1.2. The intensities of the different diffraction peaks vary widely, and are zero for some combinations of h , k , and l . For this example of polycrystalline silicon, notice the absence of all combinations of h , k , and l that are mixtures of even and odd integers, and the absence of all even integer combinations whose sum is not divisible by 4. This is the “diamond cubic structure factor rule,” discussed in Sect. 6.3.2.

One important use of x-ray powder diffractometry is for identifying unknown crystals in a sample. The idea is to match the positions and the intensities of the peaks in the observed diffraction pattern to a known pattern of peaks from a standard sample or from a calculation. There should be a one-to-one correspondence between the observed peaks and the indexed peaks in the candidate diffraction pattern. For a simple diffraction pattern as in Fig. 1.2, it is usually possible to guess the crystal structure with the help of the charts in Appendix A.1. This tentative indexing still needs to be checked. To do so, the θ -angles of the diffraction peaks are obtained, and used with (1.1) to obtain the interplanar spacing for each diffraction peak. For cubic crystals it is then possible to use (1.3) to convert each interplanar spacing into a lattice parameter, a_0 . (Non-cubic crystals usually require an iterative refinement of lattice parameters and angles.) The indexing is consistent if all peaks provide the same lattice parameter(s).

For crystals of low symmetry and with more than several atoms per unit cell, it becomes increasingly impractical to index a diffraction pattern by hand. An old and reliable approach is “fingerprinting.” The International Centre for Diffraction Data,

²Chapter 7 describes how to index diffraction patterns from single crystals.

Fig. 1.3 Diffraction pattern from an as-cast Zr–Cu–Ni–Al alloy. The smooth intensity with broad peaks around $2\theta = 38^\circ$ and 74° , is the contribution from the amorphous phase. The sharp peaks show some crystallization at the surface of the sample that was in contact with the copper mold



ICDD, maintains a database of diffraction patterns from hundreds of thousands of inorganic and organic materials [1.1]. For each material the data fields include the observed interplanar spacings for all observed diffraction peaks, their relative intensities, and their hkl indexing. Software packages are available to identify peaks in the experimental diffraction pattern, and then search the ICDD database to find candidate materials. Computerized searches for pattern matches are particularly valuable when the sample contains a mixture of unknown crystalline phases. The task of indexing a diffraction pattern is helped with information about chemical compositions and candidate crystal structures. For example, candidate phases can be identified with handbooks of phase diagrams, and their diffraction patterns found in the ICDD database.

When the sample contains multiple phases, there can be ambiguity in assigning a diffraction peak to a specific diffraction pattern, and there can be overlaps of peaks from different patterns. A computerized match of full patterns often proves helpful in such cases. Nevertheless, sometimes it is easy to distinguish individual diffraction patterns. The diffraction pattern in Fig. 1.3 was measured to determine if the surface of a glass-forming alloy had crystallized. The amorphous phase has two very broad peaks centered at $2\theta = 38^\circ$ and 74° . Sharp diffraction peaks from crystalline phases are easily distinguished. Although this crystalline diffraction pattern has not been indexed, the measurement was useful for showing that the solidification conditions were inadequate for obtaining a fully amorphous solid.

Another approach to structure determination by powder diffractometry is to calculate diffraction patterns from candidate crystal structures, and compare them to the measured diffraction patterns. Central to calculating a diffraction pattern are the structure factors of Sect. 6.3.2, which are characteristic of each crystal structure. Simple diffraction patterns (e.g., Fig. 1.2) can be calculated with a hand calculator, but structure factors for materials with more complicated unit cells require computer software. The most straightforward software packages take input files of atom positions, atom types, and x-ray wavelength, and return calculated positions and intensities of powder diffraction peaks. In an important extension of this approach, some features of the crystal structure, e.g., lattice parameters, are treated as adjustable parameters. These parameters are adjusted or “refined” as the software finds the best fit between the calculated and measured diffraction patterns (see Sect. 1.5.14).

1.1.3 Strain Effects

Internal strains in a material can change the positions and shapes of x-ray diffraction peaks. The simplest type of strain is a uniform dilatation. If all parts of the specimen are strained equally in all directions (i.e., isotropically), the effect is a small change in lattice parameter. The diffraction peaks shift in position but remain sharp. The shift of each peak, $\Delta\theta_B$, caused by a strain, $\varepsilon = \Delta d/d$, can be calculated by differentiating Bragg's law (1.1):

$$\frac{d}{dd} 2d \sin \theta_B = \frac{d}{dd} \lambda, \quad (1.5)$$

$$2 \sin \theta_B + 2d \cos \theta_B \frac{d\theta_B}{dd} = 0, \quad (1.6)$$

$$\Delta\theta_B = -\varepsilon \tan \theta_B. \quad (1.7)$$

When θ_B is small, $\tan \theta_B \simeq \theta_B$, so the strain is approximately equal to the fractional shift of the diffraction peak, although of opposite sign. For a uniform dilatation, the absolute shift of a diffraction peak in θ -angle increases strongly with the Bragg angle, θ_B .

The diffraction peaks remain sharp when the strain is the same in all crystallites, but in general there is a distribution of strains in a polycrystalline specimen. For example, some crystallites could be under compression and others under tension. The crystallites then have slightly different lattice parameters, so each would have its diffraction peaks shifted slightly in angle as given by (1.7). A distribution of strains in a polycrystalline sample therefore causes a broadening in angle of the diffraction peaks, and the peaks at higher Bragg angles are broadened more. This same argument applies when the interatomic separation depends on chemical composition—diffraction peaks are broadened when the chemical composition of a material is inhomogeneous.

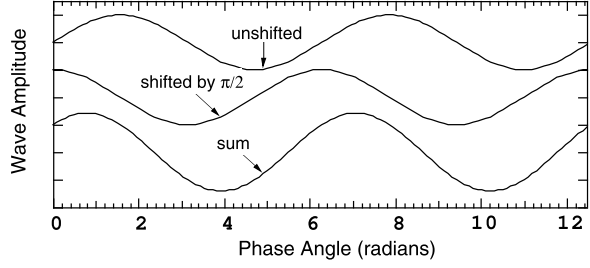
1.1.4 Size Effects

The width of a diffraction peak is affected by the number of crystallographic planes contributing to the diffraction. The purpose of this section is to show that the maximum allowed deviation from θ_B is smaller when more planes are diffracting. Diffraction peaks become sharper in θ -angle as crystallites become larger. To illustrate the principle, we consider diffraction peaks at small θ_B , so we set $\sin \theta \simeq \theta$, and linearize (1.1):³

$$2d\theta_B \simeq \lambda. \quad (1.8)$$

³This approximation will be used frequently for high-energy electrons, with their short wavelengths (for 100 keV electrons, $\lambda = 0.037 \text{ \AA}$), and hence small θ_B .

Fig. 1.4 The sum (*bottom*) of two waves out of phase by $\pi/2$. A path length difference of λ corresponds to a shift in phase angle of 2π radians or 360°



If we had only two diffracting planes, as shown in Fig. 1.1, partially-constructive wave interference occurs even for large deviations of θ from the correct Bragg angle, θ_B . In fact, for two scattered waves, errors in phase within the range $\pm 2\pi/3$ still allow constructive interference, as depicted in Fig. 1.4. This phase shift corresponds to a path length error of $\pm \lambda/3$ for the two rays in Fig. 1.1. The linearized Bragg's law (1.8) provides a range of θ angle for which constructive interference occurs:

$$\lambda - \frac{\lambda}{3} < 2d(\theta_B + \Delta\theta) < \lambda + \frac{\lambda}{3}. \quad (1.9)$$

With the range of diffraction angles allowed by (1.9), and using (1.8) as an equality, we find $\Delta\theta_{\max}$, which is approximately the largest angular deviation for which constructive interference occurs:

$$\Delta\theta_{\max} = \pm \frac{\lambda}{6d}. \quad (1.10)$$

A situation for two diffracting planes with spacing a is shown in Fig. 1.5a. The allowable error in diffraction angle, $\Delta\theta_{\max}$, becomes smaller with a larger number of diffracting planes, however. Consider the situation with 4 diffracting planes as shown in Fig. 1.5b. The total distance between the top plane and bottom plane is now 3 times larger. For the same path length error as in Fig. 1.5a, the error in diffraction angle is about 3 times smaller. For N diffracting planes (separated by a distance $d = a(N - 1)$) we have instead of (1.10):

$$\Delta\theta_{\max} \simeq \pm \frac{\lambda}{6(N - 1)a}. \quad (1.11)$$

Using (1.8) to provide the expression $\lambda/(2a) \simeq \theta_B$ for substitution into (1.11), we obtain:

$$\frac{\Delta\theta_{\max}}{\theta_B} \simeq \frac{1}{3(N - 1)}. \quad (1.12)$$

A single plane of atoms diffracts only weakly. It is typical to have hundreds of diffracting planes for high-energy electrons, and tens of thousands of planes for typical x-rays, so precise diffraction angles are possible for high-quality crystals.

It turns out that (1.12) predicts a $\Delta\theta_{\max}$ that is too small. Even if the very top-most and very bottommost planes are out of phase by more than $\lambda/3$, it is possible

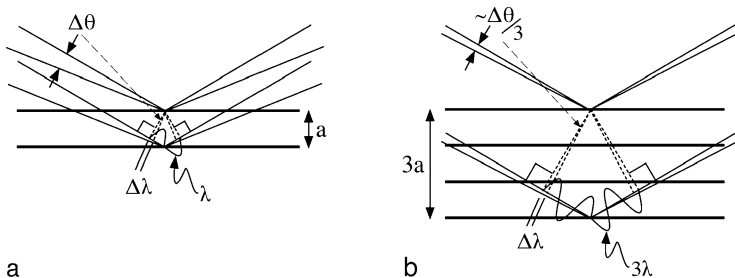


Fig. 1.5 (a) Path length error, $\Delta\lambda$, caused by error in incident angle of $\Delta\theta$. (b) Same path length error as in part (a), here caused by a smaller $\Delta\theta$ and a longer vertical distance

for most of the crystal planes to interfere constructively so that diffraction peaks still occur. For determining the sizes of crystals, a better approximation (replacing (1.12)) at small θ is:

$$\frac{\Delta\theta}{\theta_B} \simeq \frac{0.9}{N}, \quad (1.13)$$

where $\Delta\theta$ is the half-width of the diffraction peak. The approximate (1.13) must be used with caution, but it has qualitative value. It states that the number of diffracting planes is nearly equal to the ratio of the angle of the diffraction peak to the width of a diffraction peak. The widths of x-ray diffraction peaks are handy for determining crystallite sizes in the range of several nanometers (Sect. 9.1.1).

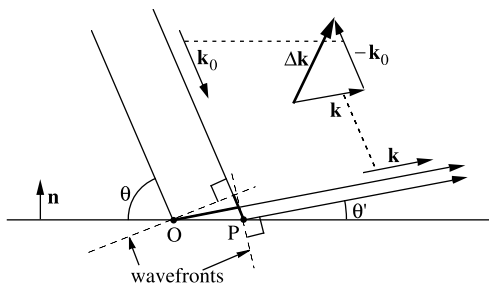
1.1.5 A Symmetry Consideration

Diffraction is not permitted in the situation shown in Fig. 1.6 with waves incident at angle θ , but scattered into an angle θ' not equal to θ . Between the two dashed lines (representing wavefronts), the path lengths of the two rays in Fig. 1.6 are unequal. When $\theta \neq \theta'$, the difference in these two path lengths is proportional to the distance between the points O and P on the scattering plane. Along a continuous plane, there is a continuous range of separations between O and P, so there is as much destructive interference as constructive interference. Strong diffraction is therefore impossible.

It will later prove convenient to formulate diffraction problems with the wavevectors, \mathbf{k}_0 and \mathbf{k} , normal to the incident and diffracted wavefronts. The \mathbf{k}_0 and \mathbf{k} have equal magnitudes, $k = 2\pi/\lambda$, because in diffraction the scattering is elastic. There is a special significance of the “diffraction vector,” $\Delta\mathbf{k} \equiv \mathbf{k} - \mathbf{k}_0$, which is shown graphically as a vector sum in Fig. 1.6. A general principle is that the diffracting material must have translational invariance in the plane perpendicular to $\Delta\mathbf{k}$. When this requirement is met, as in Fig. 1.1 but not in Fig. 1.6, diffraction experiments measure interplanar spacings along $\widehat{\Delta\mathbf{k}}$.⁴

⁴ A hat over a vector denotes a unit vector: $\hat{\mathbf{x}} \equiv \mathbf{x}/x$, where $x \equiv |\mathbf{x}|$.

Fig. 1.6 Improper geometry for diffraction with $\theta \neq \theta'$. The difference in path lengths is the difference in lengths of the two dark segments with ends at O and P. The vector $\Delta\mathbf{k}$ is the difference between the outgoing and incident wavevectors; \mathbf{n} is the surface normal. For diffraction experiments, $\mathbf{n} \parallel \Delta\mathbf{k}$



1.1.6 Momentum and Energy

The diffraction vector $\Delta\mathbf{k} \equiv \mathbf{k} - \mathbf{k}_0$, when multiplied by Planck's constant, \hbar , is the change in momentum of the x-ray after diffraction:⁵

$$\Delta\mathbf{p} = \hbar\Delta\mathbf{k}. \quad (1.14)$$

The crystal that does the diffraction must gain an equal but opposite momentum—momentum is always conserved. This momentum is eventually transferred to Earth, which undergoes a negligible change in its orbit.

Any transfer of energy to the crystal means that the scattered x-ray will have somewhat less energy than the incident energy, which might impair diffraction experiments. Consider two types of energy transfers.

First, a transfer of kinetic energy may follow the transfer of momentum of (1.14), meaning that a kinetic energy of recoil is taken up by motion of the crystal. The recoil energy is $E_{\text{recoil}} = p^2/(2M)$. If M is the mass of a modest crystal, E_{recoil} is negligible (in that it cannot be detected today without heroic effort). When diffraction occurs, the kinetic energy is transferred to all atoms in the crystal, or at least those atoms within the spatial range described in Sect. 1.1.4.

Second, energy may be transferred to a single atom, such as by moving the nucleus (causing atom vibrations), or by causing an electron of the atom to escape, ionizing the atom. A feature of quantum mechanics is that these events happen to some x-rays, but not to others. In general, the x-rays that undergo these “inelastic scattering” processes⁶ are “tagged” by one atom, and cannot participate in diffraction from a full crystal.

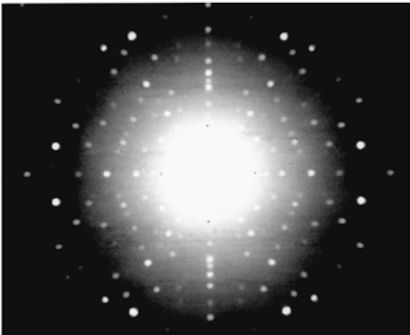
⁵This is consistent with a photon momentum of $\mathbf{p} = \hat{\mathbf{k}}E/c = \hat{\mathbf{k}}\hbar\omega/c = \hbar\mathbf{k}$, where c is the speed of light and $E = \hbar\omega$ is the photon energy.

⁶For x-rays, inelastic scattering is covered in Sect. 4.2, and parts of Chap. 5. For electrons, see Sect. 1.2 and Chap. 5, and for neutrons, see Chap. 3 and Appendix A.10.

Table 1.1 Experimental methods for diffraction

Sample	Radiation	
	monochromatic	polychromatic
single crystal	single crystal methods	Laue
polycrystal	Debye–Scherrer	none

Fig. 1.7 Backscatter Laue diffraction pattern from Si in [110] zone orientation. Notice the high symmetry of the diffraction pattern



1.1.7 Experimental Methods

The Bragg condition of (1.1) is unlikely to be satisfied for an arbitrary orientation of the crystallographic planes with respect to the incident x-ray beam, or with an arbitrary wavelength. There are three practical approaches for observing diffractions and making diffraction measurements (see Table 1.1). All are designed to ensure that Bragg’s law is satisfied. One approach, the “Debye–Scherrer” method, uses monochromatic radiation, but uses a distribution of crystallographic planes as provided by a polycrystalline sample. Another approach, the “Laue method,” uses the distribution of wavelengths in polychromatic or “white” radiation, and a single crystal sample. The combination of white radiation and polycrystalline samples produces too many diffractions, so this is not a useful technique. On the other hand, the study of single crystals with monochromatic radiation is an important technique, especially for determining the structures of minerals and large organic molecules in crystalline form.

The “Laue Method” uses a broad range of x-ray wavelengths with specimens that are single crystals. It is commonly used for determining the orientations of single crystals. With the Laue method, the orientations and positions of both the crystal and the x-ray beam are stationary. Some of the incident x-rays have the correct wavelengths to satisfy Bragg’s law for some crystal planes. In the Laue diffraction pattern of Fig. 1.7, the different diffraction spots along a radial row originate from various combinations of x-ray wavelengths and crystal planes having a projected normal component along the row. It is not easy to evaluate these combinations (especially when there are many orientations of crystallites in the sample), and the Laue method will not be discussed further.

Fig. 1.8 Arrangement for Debye–Scherrer diffraction from a polycrystalline sample

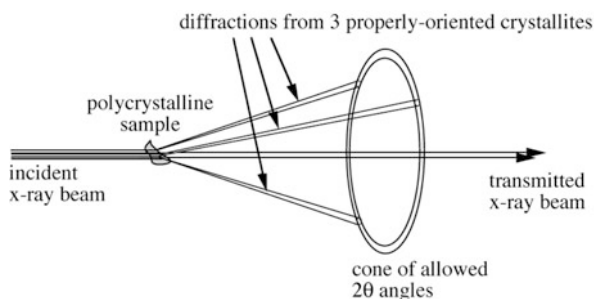
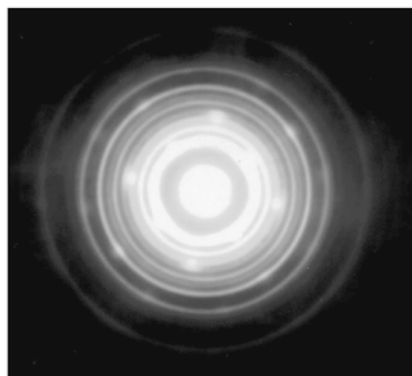


Fig. 1.9 Superimposed electron diffraction patterns from polycrystalline Ni–Zr and single crystal NaCl



The “Debye–Scherrer” method uses monochromatic x-rays, and equipment to control the 2θ angle for diffraction. The Debye–Scherrer method is most appropriate for polycrystalline samples. Even when θ is a Bragg angle, however, the incident x-rays are at the wrong angle for most of the crystallites in the sample (which may have their planes misoriented as in Fig. 1.6, for example). Nevertheless, when θ is a Bragg angle, in most powders there are some crystallites oriented adequately for diffraction. When enough crystallites are irradiated by the beam, the crystallites diffract the x-rays into a set of diffraction cones as shown in Fig. 1.8. The apex angles of the diffraction cones are $4\theta_B$, where θ_B is the Bragg angle for the specific diffraction.

Debye–Scherrer diffraction patterns are also obtained by diffraction of monochromatic electrons from polycrystalline specimens. Two superimposed electron diffraction patterns are presented in Fig. 1.9. The sample was a crystalline Ni–Zr alloy deposited as a thin film on a single crystal of NaCl. The polycrystalline Ni–Zr gave a set of diffraction cones as in Fig. 1.8. These cones were oriented to intersect a sheet of film in the transmission electron microscope, thus forming an image of “diffraction rings.” A square array of diffraction spots is also seen in Fig. 1.9. These spots originate from some residual NaCl that remained on the sample, and the spots form a single crystal diffraction pattern.

Diffraction from polycrystalline materials, or “powder diffraction” with monochromatic radiation, requires the Debye–Scherrer diffractometer to provide only one

degree of freedom in changing the diffraction conditions, corresponding to changing the 2θ angle of Figs. 1.1–1.3. On the other hand, three additional degrees of freedom for specimen orientation are required for single crystal diffraction experiments with monochromatic radiation. Although diffractions from single crystals are more intense, these added parametric dimensions require a considerable increase in data measurement time. Such measurements are possible with equipment in a small laboratory, but bright synchrotron radiation sources have enabled many new types of single crystal diffraction experiments.

1.2 The Creation of X-Rays

X-rays are created when energetic electrons lose energy. The same processes of x-ray creation are relevant for obtaining x-rays in an x-ray diffractometer, and for obtaining x-rays for chemical analysis in an analytical transmission electron microscope. Some relevant electron-atom interactions are summarized in Fig. 1.10. Figure 1.10a shows the process of elastic scattering where the electron is deflected, but no energy loss occurs. Elastic scattering is the basis for electron diffraction. Figure 1.10b is an inelastic scattering where the deflection of the electron results in radiation. The acceleration during the deflection of a classical electron would always produce radiation, and hence no elastic scattering. In quantum electrodynamics the radiation may or may not occur (compare Figs. 1.10a and 1.10b), but the average over many electron scatterings corresponds to the classical radiation field.

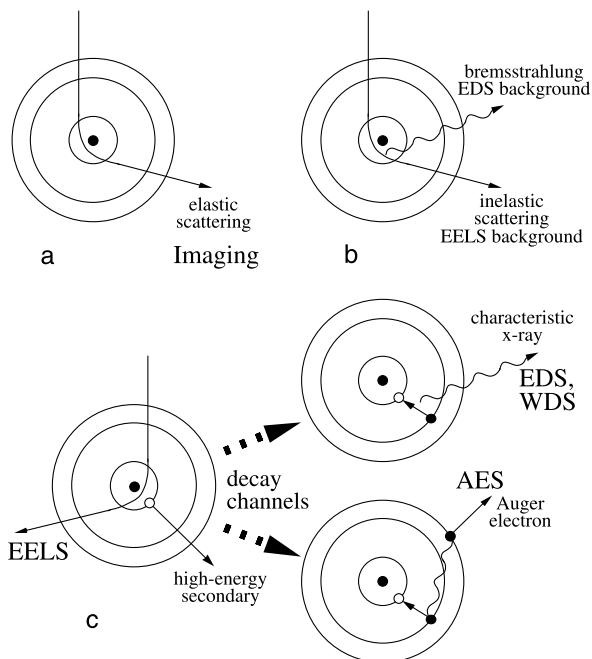
Figure 1.10c illustrates two processes involving energy transfer between the incident electron and the electrons of the atom. Both processes of Fig. 1.10c involve a primary ionization where a core electron is ejected from the atom. An outer electron of more positive energy falls into this core hole, but there are two ways to dispose of its excess energy: 1) an x-ray can be emitted directly from the atom, or 2) this energy can be used to eject another outer electron from the atom, called an “Auger electron.” The “characteristic x-ray” of process 1 carries the full energy difference of the two electron states. The Auger electron was originally bound to the atom, however, so the kinetic energy of the emitted Auger electron is this energy difference minus its initial binding energy. After either decay process of Fig. 1.10c, there remains an empty electron state in an outer shell of the atom, and the process repeats itself at a lower energy until the electron hole migrates out of the atom.

An x-ray for a diffraction experiment is characterized by its wavelength, λ , whereas for spectrometry or x-ray creation the energy, E , is typically more useful. The two are related inversely, and (1.16) is worthy of memorization:

$$E = h\nu = h\frac{c}{\lambda}, \quad (1.15)$$

$$E [\text{keV}] = \frac{12.3984}{\lambda [\text{\AA}]} \simeq \frac{12.4}{\lambda [\text{\AA}]}. \quad (1.16)$$

Fig. 1.10 (a)–(c) Some processes of interaction between a high-energy electron and an atom: (a) is useful for diffraction, whereas the ejection of a core electron in (c) is the basis for chemical spectroscopies. Two decay channels for the core hole in (c) are indicated by the two thick, dashed arrows



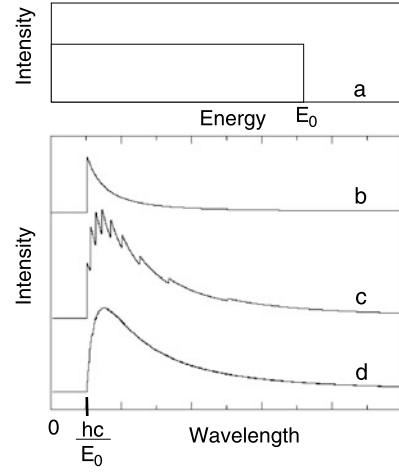
1.2.1 Bremsstrahlung

Continuum radiation (somewhat improperly called bremsstrahlung, meaning “braking radiation”) can be emitted when an electron undergoes a strong deflection as depicted in Fig. 1.10b, because the deflection causes an acceleration. This acceleration can create an x-ray with an energy as high as the full kinetic energy of the incident electron, E_0 (equal to its charge, e , times its accelerating voltage, V). Substituting $E_0 = eV$ into (1.15), we obtain the “Duane–Hunt rule” for the shortest x-ray wavelength from the anode, λ_{\min} :

$$\frac{hc}{eV} = \lambda_{\min} [\text{\AA}] = \frac{12.3984}{E_0 [\text{keV}]} \quad (1.17)$$

The shape of the bremsstrahlung spectrum can be understood by using one fact from quantum electrodynamics. Although each x-ray photon has a distinct energy, the photon energy spectrum is obtained from the Fourier transform of the time dependence of the electron acceleration, $a(t)$. The passage of each electron through an atom provides a brief, pulse-type acceleration. The average over many electron-atom interactions provides a broadband x-ray energy spectrum. Electrons that pass closer to the nucleus undergo stronger accelerations, and hence radiate with a higher probability. Their spectrum, however, is the same as the spectrum from electrons that traverse the outer part of an atom. In a thin specimen where only one sharp acceleration of the electron can take place, the bremsstrahlung spectrum has an en-

Fig. 1.11 (a) Energy distribution for single bremsstrahlung process. (b) Wavelength distribution for the energy distribution of part (a). (c) Coarse-grained sum of wavelength distributions expected from multiple bremsstrahlung processes in a thick target (d) sum of contributions from single bremsstrahlung processes of a continuous energy distribution



ergy distribution shown in Fig. 1.11a; a flat distribution with a cutoff of 40 keV for electrons of 40 keV.

The general shape of the wavelength distribution can be understood as follows. The energy-wavelength relation for the x-ray is:

$$\nu = \frac{E}{h} = \frac{c}{\lambda}, \quad (1.18)$$

so an interval in wavelength is related to an interval in energy as:

$$\frac{dE}{d\lambda} = -ch \frac{1}{\lambda^2}, \quad (1.19)$$

$$dE = -\frac{ch}{\lambda^2} d\lambda. \quad (1.20)$$

The same number of photons must be counted in the interval of the wavelength distribution that corresponds to an interval in the energy distribution:

$$I(\lambda) d\lambda = I(E) dE, \quad (1.21)$$

so by using (1.19), the wavelength distribution is:

$$I(\lambda) d\lambda = -I(E) \frac{ch}{\lambda^2} d\lambda. \quad (1.22)$$

The negative sign in (1.22) appears because an increase in energy corresponds to a decrease in wavelength. The wavelength distribution is therefore related to the energy distribution as:

$$I(\lambda) = ch \frac{I(E)}{\lambda^2}. \quad (1.23)$$

Figure 1.11b is the wavelength distribution (1.23) that corresponds to the energy distribution of Fig. 1.11a. Notice how the bremsstrahlung x-rays have wavelengths bunched towards the value of λ_{\min} of (1.17).

The curve in Fig. 1.11b, or its equivalent energy spectrum in Fig. 1.11a, is a reasonable approximation to the bremsstrahlung background from a very thin specimen. The anode of an x-ray tube is rather thick, however. Most electrons do not lose all their energy at once, and propagate further into the anode. When an electron has lost some of its initial energy, it can still radiate again, but with a smaller E_{\max} (or larger λ_{\min}). Deeper within the anode, these multiply-scattered electrons emit more bremsstrahlung of longer wavelengths. The spectrum of bremsstrahlung from a thick sample can be understood by summing the individual spectra from electrons of various kinetic energies in the anode. A coarse sum is presented qualitatively in Fig. 1.11c, and a higher resolution sum is presented in Fig. 1.11d. The bremsstrahlung from an x-ray tube increases rapidly above λ_{\min} , reaching a peak at about $1.5\lambda_{\min}$.⁷

The intensity of the bremsstrahlung depends on the strength of the accelerations of the electrons. Atoms of larger atomic number, Z , have stronger potentials for electron scattering, and the intensity of the bremsstrahlung increases approximately as $V^2 Z^2$.

1.2.2 Characteristic Radiation

In addition to the bremsstrahlung emitted when a material is bombarded with high-energy electrons, x-rays are also emitted with discrete energies characteristic of the elements in the material, as depicted in Fig. 1.10c (top part). The energies of these “characteristic x-rays” are determined by the binding energies of the electrons of the atom, or more specifically the differences in these binding energies. It is not difficult to calculate these energies for atoms of atomic number, Z , if we make the major assumption that the atoms are “hydrogenic” and have only one electron. We seek solutions to the time-independent Schrödinger equation for the electron wavefunction:

$$-\frac{\hbar^2}{2m}\nabla^2\psi(r, \theta, \phi) - \frac{Ze^2}{r}\psi(r, \theta, \phi) = E\psi(r, \theta, \phi). \quad (1.24)$$

To simplify the problem, we seek solutions that are spherically symmetric, so the derivatives of the electron wavefunction, $\psi(r, \theta, \phi)$, are zero with respect to the angles θ and ϕ of our spherical coordinate system. In other words, we consider cases where the electron wavefunction is a function of r only: $\psi(r)$. The Laplacian

⁷The continuum spectrum of Fig. 1.11d is correct qualitatively, but a quantitative analysis requires more details about electron scattering and x-ray absorption.

in the Schrödinger equation then takes a relatively simple form:

$$-\frac{\hbar^2}{2m} \frac{1}{r^2} \frac{\partial}{\partial r} \left(r^2 \frac{\partial}{\partial r} \psi(r) \right) - \frac{Ze^2}{r} \psi(r) = E \psi(r). \quad (1.25)$$

Since E is a constant, acceptable expressions for $\psi(r)$ must provide an E that is independent of r . Two such solutions are:

$$\psi_{1s}(r) = e^{-\frac{Zr}{a_0}}, \quad (1.26)$$

$$\psi_{2s}(r) = \left(2 - \frac{Zr}{a_0} \right) e^{-\frac{Zr}{2a_0}}, \quad (1.27)$$

where the Bohr radius, a_0 , is defined as:

$$a_0 = \frac{\hbar^2}{me^2}. \quad (1.28)$$

By substituting (1.26) or (1.27) into (1.25), and taking the partial derivatives with respect to r , it is found that the r -dependent terms cancel out, leaving E independent of r (see Problem 1.7):

$$E_n = -\frac{1}{n^2} Z^2 \left(\frac{me^4}{2\hbar^2} \right) = -\frac{1}{n^2} Z^2 E_R. \quad (1.29)$$

In (1.29) we have defined the energy unit, E_R , the Rydberg, which is +13.6 eV. The integer, n , in (1.29) is sometimes called the “principal quantum number,” which is 1 for ψ_{1s} , 2 for ψ_{2s} , etc. It is well-known that there are other solutions for ψ that are not spherically-symmetric, for example, ψ_{2p} , ψ_{3p} , and ψ_{3d} .⁸ Perhaps surprisingly, for ions having a single electron, (1.29) provides the correct energies for these other electron wavefunctions, where $n = 2, 3$, and 3 for these three examples. This is known as an “accidental degeneracy” of the Schrödinger equation for the hydrogen atom, but it is not true when there is more than one electron about the atom.

Suppose a Li atom with $Z = 3$ has been stripped of both its inner $1s$ electrons, and suppose an electron in a $2p$ state undergoes an energetically downhill transition into one of these empty $1s$ states. The energy difference can appear as an x-ray of

⁸The time-independent Schrödinger equation (1.24) was obtained by the method of separation of variables, specifically the separation of t from r, θ, ϕ . The constant of separation was the energy, E . For the separation of θ and ϕ from r , the constant of separation provides l , and for the separation of θ from ϕ , the constant of separation provides m . The integers l and m involve the angular variables θ and ϕ , and are “angular momentum quantum numbers.” The quantum number l corresponds to the total angular momentum, and m corresponds to its orientation along a given direction. The full set of electron quantum numbers is $\{n, l, m, s\}$, where s is spin. Spin cannot be obtained from a constant of separation of the Schrödinger equation, which offers only 3 separations for $\{r, \theta, \phi, t\}$. Spin is obtained from the relativistic Dirac equation, however.

energy ΔE , and for this 1-electron atom it is:

$$\Delta E = E_2 - E_1 = -\left(\frac{1}{2^2} - \frac{1}{1^2}\right)Z^2 E_R = \frac{3}{4}Z^2 E_R. \quad (1.30)$$

(The $1s$ state, closer to the nucleus than the $2p$ state, has the more negative energy. The x-ray has a positive energy.) A standard old notation groups electrons with the same n into “shells” designated by the letter series K, L, M, \dots corresponding to $n = 1, 2, 3, \dots$. The electronic transition of (1.30) between shells $L \rightarrow K$ emits a “ $K\alpha$ x-ray.” A $K\beta$ x-ray originates with the transition $M \rightarrow K$. Other designations are given in Table 1.2 and Fig. 1.13.

Equation (1.30) works well for x-ray emission from atoms or ions having only one electron, but electron-electron interactions complicate the calculation of energy levels of most atoms.⁹ Figure 1.12 shows bands of data, which originate with electronic transitions between different shells. This plot of the relationship between the atomic number and the x-ray energy is the basis for Moseley’s laws. Moseley’s laws are modifications of (1.30). For $K\alpha$ and $L\alpha$ x-rays, they are:

$$E_{K\alpha} = (Z - 1)^2 E_R \left(\frac{1}{1^2} - \frac{1}{2^2} \right) = 10.204(Z - 1)^2, \quad (1.31)$$

$$E_{L\alpha} = (Z - 7.4)^2 E_R \left(\frac{1}{2^2} - \frac{1}{3^2} \right) = 1.890(Z - 7.4)^2. \quad (1.32)$$

Equations (1.31) and (1.32) are good to about 1 % accuracy for x-rays with energies from 3–10 keV.¹⁰

Moseley correctly interpreted the offsets for Z (1 and 7.4 in (1.31) and (1.32)) as originating from shielding of the nuclear charge by other core electrons. For an electron in the K -shell, the shielding involves one electron—the other electron in the K -shell. For an electron in the L -shell, shielding involves both K electrons ($1s$) plus to some extent the other L electrons ($2s$ and $2p$), which is a total of 9. Perhaps Moseley’s law of (1.31) for the $L \rightarrow K$ transition could be rearranged with different effective nuclear charges for the K and L -shell electrons, rather than using $Z - 1$ for both of them. This change would, however, require a constant different from E_R in (1.31). The value of 7.4 for L -series x-rays, in particular, should be regarded as an empirical parameter.

Notice that Table 1.2 and Fig. 1.13 do not include the transition $2s \rightarrow 1s$. This transition is forbidden. The two wavefunctions, $\psi_{1s}(r)$ and $\psi_{2s}(r)$ of (1.26) and (1.27), have inversion symmetry about $r = 0$. A uniform electric field is antisymmetric in \mathbf{r} , however, so the induced dipole moment of $\psi_{2s}(r)$ has zero net overlap

⁹Additional electron-electron potential energy terms are needed in (1.24), and these alter the energy levels.

¹⁰This result was published in 1914. Henry Moseley died in 1915 at Gallipoli during World War I. The British response to this loss was to assign scientists to noncombatant duties during World War II.

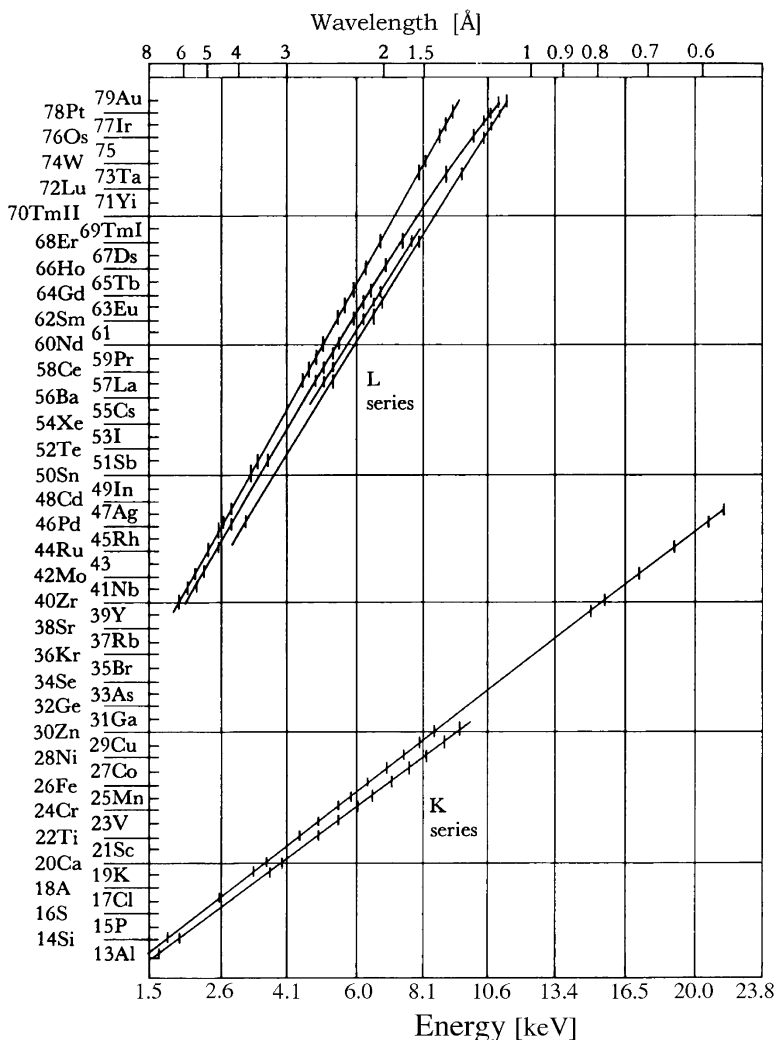


Fig. 1.12 Characteristic x-ray energies of the elements. The x-axis of plot was originally the square root of frequency (from 6 to $24 \times 10^8 \sqrt{\text{Hz}}$) [1.2]

with $\psi_{1s}(r)$. X-ray emission by electric dipole radiation is subject to a selection rule (see Problem 1.12), where the angular momentum of the initial and final states must differ by 1 (i.e., $\Delta l = \pm 1$).

As shown in Table 1.2, there are two types of $K\alpha$ x-rays. They differ slightly in energy (typically by parts per thousand), and this originates from the spin-orbit splitting of the L shell. Recall that the $2p$ state can have a total angular momentum of $3/2$ or $1/2$, depending on whether the electron spin of $1/2$ lies parallel or antiparallel to the orbital angular momentum of 1. The spin-orbit interaction causes

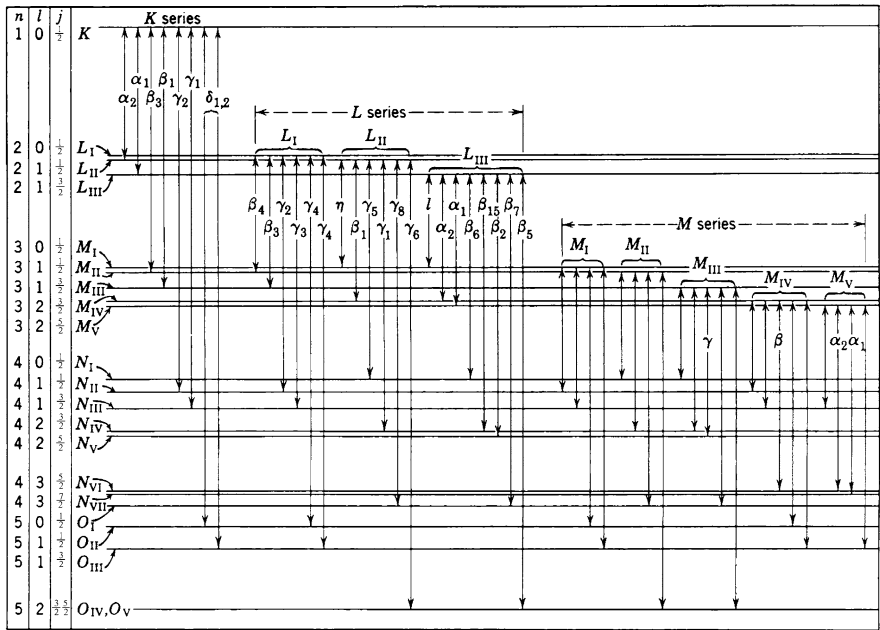


Fig. 1.13 Some electron states and x-ray notation (in this case for U). After [1.3]

Table 1.2 Some x-ray spectroscopic notations

Label	Transition	Atomic notation	E for Cu [keV]
$K\alpha_1$	$L_3 \rightarrow K$	$2p^{3/2} \rightarrow 1s$	8.04778
$K\alpha_2$	$L_2 \rightarrow K$	$2p^{1/2} \rightarrow 1s$	8.02783
$K\beta_{1,3}$	$M_{2,3} \rightarrow K$	$3p \rightarrow 1s$	8.90529
$K\beta_5$	$M_{4,5} \rightarrow K$	$3d \rightarrow 1s$	8.99770
$L\alpha_{1,2}$	$M_{4,5} \rightarrow L_3$	$3d \rightarrow 2p^{3/2}$	0.9297
$L\beta_1$	$M_4 \rightarrow L_2$	$3d \rightarrow 2p^{1/2}$	0.9498
$L\beta_{3,4}$	$M_{2,3} \rightarrow L_1$	$3p \rightarrow 2s$	1.0228
$L\eta$	$M_1 \rightarrow L_2$	$3s \rightarrow 2p^{1/2}$	0.832
L_l	$M_1 \rightarrow L_3$	$3s \rightarrow 2p^{3/2}$	0.8111

the 1/2 state (L_2) to lie at a lower energy than the 3/2 state (L_3), so the $K\alpha_1$ x-ray is slightly more energetic than the $K\alpha_2$ x-ray. There is no spin-orbit splitting of the final K -states since their orbital angular momentum is zero, but spin-orbit splitting occurs for the final states of the $M \rightarrow L$ x-ray emissions. The $L\alpha_1$ and $L\beta_1$ x-rays are differentiated in this way, as shown in Table 1.2. Subshell splittings may not be resolved in experimental energy spectra, and it may be possible to identify only a composite $K\beta$ x-ray peak, for example.

1.2.3 Synchrotron Radiation

Storage Rings Synchrotron radiation is a practical source of x-rays for many experiments that are impractical with the conventional x-ray sources of Sect. 1.3.1. High flux and collimation, energy tunability, and timing capabilities are some special features of synchrotron radiation sources. Facilities for synchrotron radiation experiments are available at several national or international laboratories.¹¹ These facilities are centered around an electron (or positron) storage ring with a circumference of about one kilometer. The electrons in the storage ring have energies of typically 7×10^9 eV, and travel close to the speed of light. The electron current is perhaps 100 mA, but the electrons are grouped into tight bunches of centimeter length, each with a fraction of this total current. The bunches have vertical and horizontal spreads of tens of microns.

The electrons lose energy by generating synchrotron radiation as they are bent around the ring. These energy losses are primarily in the electron mass, not velocity (which stays close to the speed of light), so the bunches remain intact. The electrical power needed to replenish the energy of the electrons is provided by a radiofrequency electric field. This cyclic electric field accelerates the electron bunches by alternately attracting and repelling them as they move through a dedicated section of the storage ring. (Each bunch must be in phase with the radiofrequency field.) The ring is capable of holding a number of bunches equal to the radiofrequency times the cycle time around the ring. For example, with a 0.3 GHz radiofrequency, an electron speed of 3×10^5 km/s, and a ring circumference of 1 km, the number of “buckets” to hold the bunches is 1,000.

Although the energy of the electrons in the ring is restored by the high power radiofrequency system, electrons are lost by occasional collisions with gas atoms in the vacuum. The characteristic decay of the beam current over several hours requires that new electrons are injected into the bunches.

As the bunches pass through bending magnets or magnetic “insertion devices,” their accelerations cause photon emission. X-ray emission therefore occurs in pulsed bursts, or “flashes.” The flash duration depends on the duration of the electron acceleration, but this is shortened by relativistic contraction. The flash duration depends primarily on the width of the electron bunch, and may be 0.1 ns. In a case where every fiftieth bucket is filled in our hypothetical ring, these flashes are separated in time by 167 ns. Some experiments based on fast timing are designed around this time structure of synchrotron radiation.

Undulators Synchrotron radiation is generated by the dipole bending magnets used for controlling the electron orbit in the ring, but all modern “third generation” synchrotron radiation facilities derive their x-ray photons from “insertion devices,”

¹¹Three premier facilities are the European Synchrotron Radiation Facility in Grenoble, France, the Advanced Photon Source at Argonne, Illinois, USA, and the Super Photon Ring 8-GeV, SPring-8 in Harima, Japan [1.4].

which are magnet structures such as “wigglers” or “undulators.” Undulators comprise rows of magnets along the path of the electron beam. The fields of these magnets alternate up and down, perpendicular to the direction of the electron beam. Synchrotron radiation is produced when the electrons accelerate under the Lorentz forces of the row of magnets. The mechanism of x-ray emission by electron acceleration is essentially the same as that of bremsstrahlung radiation, which was described in Fig. 1.10 and Sect. 1.2.1. Because the electron accelerations lie in a plane, the synchrotron x-rays are polarized with \mathbf{E} in this same plane and perpendicular to the direction of the x-ray (cf., Fig. 1.26).

The important feature of an undulator is that its magnetic fields are positioned precisely so that the photon field is built by the constructive interference of radiation from a row of accelerations. The x-rays emerge from the undulator in a tight pattern analogous to a Bragg diffraction from a crystal, where the intensity of the x-ray beam in the forward direction increases as the square of the number of coherent magnetic periods (typically tens). Again in analogy with Bragg diffraction, there is a corresponding decrease in the angular spread of the photon beam. The relativistic nature of the GeV electrons is also central to undulator operation. In the line-of-sight along the electron path, the electron oscillation frequency is enhanced by the relativistic factor $2(1 - (v/c)^2)^{-1/2}$, where v is the electron velocity and c is the speed of light. This factor is about 10^8 for electron energies of several GeV. Typical spacings of the magnets are 3 cm, a distance traversed by light in 10^{-10} s. The relativistic enhancement brings the frequency to 10^{18} Hz, which corresponds to an x-ray energy, $h\nu$, of several keV. The relativistic Lorentz contraction along the forward direction further sharpens the radiation pattern. The x-ray beam emerging from an undulator may have an angular spread of microradians, diverging by only a millimeter over distances of tens of meters. A small beam divergence and a small effective source area for x-ray emission makes an undulator beam an excellent source of x-rays for operating a monochromator.

Brightness Various figures of merit describe how x-ray sources provide useful photons. The figure of merit for operating a monochromator is proportional to the intensity (photons/s) per area of emitter (cm^{-2}), but another factor also must be included. For a highly collimated x-ray beam, the monochromator crystal is small compared to the distance from the source. It is important that the x-ray beam be concentrated into a small solid angle so it can be utilized effectively. The full figure of merit for monochromator operation is “brightness” (often called “brilliance”), which is normalized by the solid angle of the beam. Brightness has units of $[\text{photons} (\text{s cm}^2 \text{ sr})^{-1}]$. The brightness of an undulator beam can be 10^9 times that of a conventional x-ray tube. Brightness is also a figure of merit for specialized beamlines that focus an x-ray beam into a narrow probe of micron dimensions. Finally, the x-ray intensity is not distributed uniformly over all energies. The term “spectral brilliance” is a figure of merit that specifies brightness per eV of energy in the x-ray spectrum.

Undulators are tuneable to optimize their output within a broad energy range. Their power density is on the order of kW mm^{-2} , and much of this energy is de-

posited as heat in the first crystal that is hit by the undulator beam. There are technical challenges in extracting heat from the first crystal of this “high heat load monochromator.” It may be constructed for example, of water-cooled diamond, which has excellent thermal conductivity.

Beamlines and User Programs The monochromators and goniometers needed for synchrotron radiation experiments are located in a “beamline,” which is along the forward direction from the insertion device. These components are typically mounted in lead-lined “hutches” that shield users from the lethal radiation levels produced by the undulator beam.

Synchrotron radiation user programs are typically organized around beamlines, each with its own capabilities and scientific staff. Although many beamlines are dedicated to x-ray diffraction experiments, many other types of x-ray experiments are possible. Work at a beamline requires success with a formal proposal for an experiment. This typically begins by making initial contact with the scientific staff at the beamline, who can often give a quick assessment of feasibility and originality. Successful beamtime proposals probably will not involve measurements that can be performed with conventional x-ray diffractometers. Radiation safety training, travel arrangements, operating schedules and scientific collaborations are issues for experiments at synchrotron facilities. The style of research differs considerably from that with a diffractometer in a small laboratory.

1.3 The X-Ray Powder Diffractometer

This section describes the essential components of a typical x-ray diffractometer used in a materials analysis laboratory:

- a source of x-rays, usually a sealed x-ray tube,
- a “goniometer,” which provides precise mechanical motions of the tube, specimen, and detector,
- an x-ray detector,
- electronics for counting detector pulses in synchronization with the positions of the goniometer.

Typical data comprise a list of detector counts versus 2θ angle, whose graph is the diffraction pattern.

1.3.1 Practice of X-Ray Generation

Conventional x-ray tubes are vacuum tube diodes, with their filaments biased typically at -40 kV. Electrons are emitted thermionically from the filament, and ac-

celerate into the anode, which is maintained at ground potential.¹² Analogous components are used in an analytical TEM (Sect. 2.4.1), although the electron energies are higher, the electron beam can be shaped into a finely-focused probe, and the electrons induce x-ray emission from the specimen.

The operating voltage and current of an x-ray tube are typically selected to optimize the emission of characteristic radiation, since this is a source of monochromatic radiation. For a particular accelerating voltage, the intensity of all radiations increases with the electron current in the tube. The effect of accelerating voltage on characteristic x-ray emission is more complicated, however, since the spectrum of x-rays is affected. Characteristic x-rays are excited more efficiently with higher accelerating voltage, V . In practice the intensity of characteristic radiation depends on V as:

$$I_{\text{char}} \propto (V - V_c)^{1.5}, \quad (1.33)$$

where V_c is the energy of the characteristic x-ray. On the other hand, the intensity of the bremsstrahlung increases approximately as:

$$I_{\text{brem}} \propto V^2 Z^2. \quad (1.34)$$

To maximize the characteristic x-ray intensity with respect to the continuum, we set:

$$\frac{d}{dV} \frac{I_{\text{char}}}{I_{\text{brem}}} = \frac{d}{dV} \frac{(V - V_c)^{1.5}}{V^2} = 0, \quad (1.35)$$

which provides:

$$V = 4V_c. \quad (1.36)$$

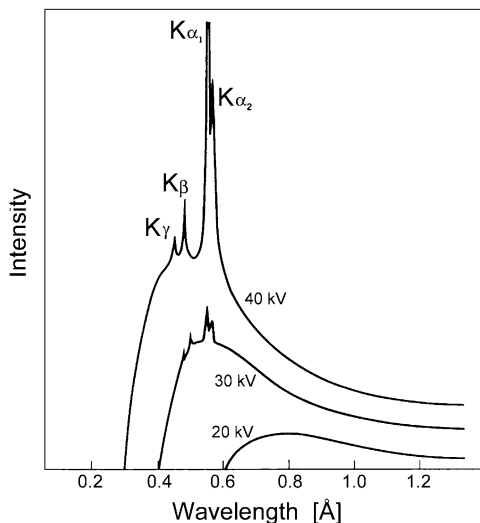
In practice, the optimal voltage for exciting the characteristic x-rays is about 3.5–4 times the energy of the characteristic x-ray.

Combining the bremsstrahlung and characteristic x-ray intensities gives wavelength distributions as shown in Fig. 1.14. For this example of an x-ray tube with a silver anode, the characteristic $K\alpha$ lines (22.1 keV, 0.56 Å) are not excited at tube voltages below 25.6 keV, which corresponds to the energy required to remove a K -shell electron from a silver atom. Maximizing the ratio of characteristic silver $K\alpha$ intensity to bremsstrahlung intensity would require an accelerating voltage around 100 keV, which is impractically high. The most popular anode material for monochromatic radiation is copper, which also provides the benefit of high thermal conductivity.

A modern sealed x-ray tube has a thin anode with cooling water flowing behind it. If the anode has good thermal conduction, as does copper, perhaps 2 kW of power

¹²The alternative arrangement of having the filament at ground and the anode at +40 kV is incompatible with water cooling of the anode. Cooling is required because a typical electron current of 25 mA demands the dissipation of 1 kW of heat from a piece of metal situated in a high vacuum. In a TEM, it is also convenient to keep the specimen and most components at ground potential.

Fig. 1.14 Intensity spectrum (in wavelength) of an x-ray tube with a silver anode [1.5]. Energies of 20, 30, 40 keV correspond to cutoff wavelengths of 0.62, 0.41, 0.32 Å, respectively



(accelerating voltage times beam current) can be used before anode heating shortens excessively the tube life.¹³ An alternative type of x-ray tube has been developed to handle higher electron currents, and hence proportionately more x-ray emission. The trick is to construct the anode as a cylinder, and spin it at about 5,000 RPM during operation. Higher heat dissipations are possible with these rotating anode x-ray sources, perhaps 20 kW. Rotating anode x-ray sources are more expensive and complicated, however, because they require high mechanical precision in the rotating components, a leak-proof high vacuum rotating seal with provisions for water cooling, and continuous vacuum pumping. Both rotating anode and sealed tube x-ray sources require a regulated high voltage dc power supply for their operation. These high voltage generators include a feedback control circuit to adjust the thermionic emission from the filament to maintain a steady electron current in the tube.

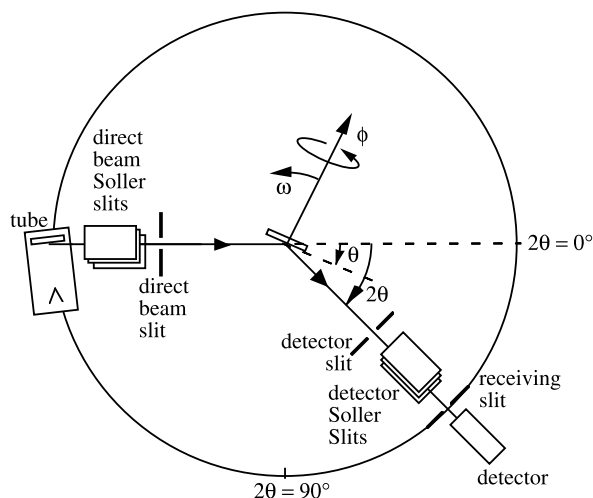
By using a direct beam slit (Fig. 1.15), a narrow x-ray beam can be obtained. By choosing this beam to be those x-rays that leave the anode surface at a shallow angle, geometrical foreshortening of the anode can be used to provide a line source. This shallow “take-off angle” of the x-ray tube is typically 3–6 degrees.

1.3.2 Goniometer for Powder Diffraction

The Debye–Scherrer method requires a “goniometer” that performs precise mechanical movements of the detector and specimen with respect to the source of

¹³The efficiency of x-ray emission, the ratio of emitted x-ray power to electrical power dissipated in the tube, ϵ , is quite low. Empirically it is found that $\epsilon = 1.4 \times 10^{-9} ZV$, where Z is the atomic number and V is accelerating voltage.

Fig. 1.15 Schematic diagram of some typical components and angles of the goniometer for a θ - 2θ x-ray diffractometer. The flat specimen is at the center of the goniometer circle, whose radius is typically 0.25–0.5 m



monochromatic x-rays (see Fig. 1.15). In practice, it is easiest to keep the bulky x-ray tube stationary, and rotate the specimen by the angle θ . To ensure that the scattered x-rays leave the specimen at angle θ , the detector must be rotated precisely by the angle 2θ .¹⁴ The goniometer may also provide for the rotation of the specimen in the plane of its surface by the angle ϕ , and in the plane of the goniometer by the angle ω . The angles ϕ and ω do not affect the diffraction pattern for a polycrystal with random orientations, but they are important for samples with crystallographic texture.

To obtain good intensity, but well-defined diffraction angles, x-ray powder diffractometers usually employ a “line source,” which is narrow in the plane of the goniometer, but has a height of perhaps 1 cm perpendicular to this plane. Slits are used to collimate the incident and diffracted beams. The direct beam slit controls the “equatorial divergence” of the incident beam (the equatorial plane of the diffractometer is in the plane of the paper of Fig. 1.15). The divergence of the incident beam along the axis of the goniometer (perpendicular to the plane of the paper) must also be controlled to obtain well-defined diffraction angles. Control of “axial divergence” is achieved with Soller slits, which are stacked plates that slice the incident beam into a stack of beams, each with low axial divergence. Between the specimen and the detector is a detector slit to control equatorial divergence, and Soller slits to control axial divergence. The position of the detector is defined by the receiving slit.

A divergent incident beam is a practical necessity for obtaining reasonable x-ray intensities at the detector. It would be unfortunate if the diffraction peaks were broadened in angle by the equatorial divergence of the incident beam, typically 1° . Fortunately, such broadening does not occur for the θ - 2θ goniometer of

¹⁴This “ θ - 2θ diffractometer” is less versatile than a “ θ - θ diffractometer,” but the latter instrument requires precise movement of its x-ray tube.

Fig. 1.16 Geometry of a Bragg–Brentano diffractometer. The two angles at the specimen are the same $180^\circ - 2\theta$

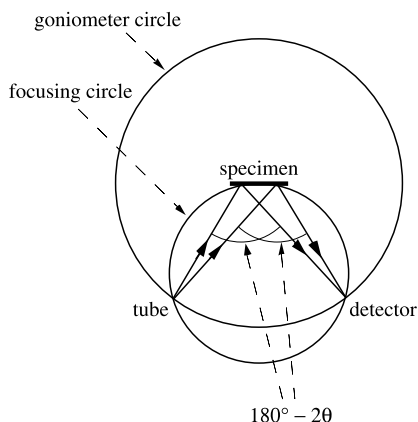


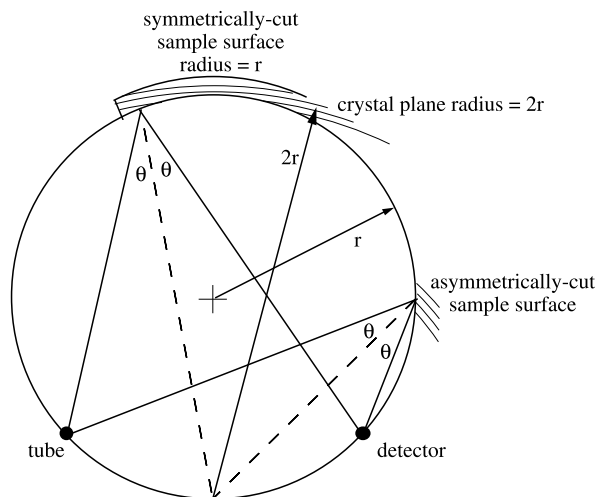
Fig. 1.15, which has “Bragg–Brentano” geometry. Bragg–Brentano geometry gives well-defined diffraction angles for finite slit widths and beam divergences, as shown with the aid of Figs. 1.16 and 1.17. In this goniometer, both detector and tube are on the circumference of a “goniometer circle” with the specimen in the center, as shown in Fig. 1.16. The beam divergence is indicated in Fig. 1.16 by the two ray paths from the tube to the detector. Although the two rays from the x-ray tube are incident at different angles on the specimen surface, if they pass through the receiving slit they form the same angle, $180^\circ - 2\theta$, at the specimen. The Bragg–Brentano geometry illuminates a reasonable area of the specimen surface, and many ray paths have the same scattering angle. Good intensity and good instrument resolution are both achieved for powder samples.

Further details of the focusing circle are shown in Fig. 1.17. It can be proved (see Problem 1.6) that the two ray paths from tube to detector make the same angle at the focusing circle (the angle $180^\circ - 2\theta$ of Fig. 1.16). It is also true that the dashed lines in Fig. 1.17, which bisect this angle, intersect at the bottom of the focusing circle, symmetrically between the tube and the detector. The dashed lines are normal to the diffracting planes. For strong diffraction, therefore, the optimal radius of curvature of the diffracting planes should be twice that of the focusing circle, and the sample surface should be curved along the focusing circle as shown in Fig. 1.17. Such crystals, known as “Johansson-cut” crystals, are specially prepared for x-ray optical devices, especially monochromators as discussed in Sects. 1.2.3 and 1.3.3.

The geometry of Fig. 1.17 is the basis for the design of a high efficiency instrument known as a Seemann–Bohlin diffractometer. In this instrument a powder or thin-film sample is spread over much of the circumference of the focusing circle. All divergent beams from the tube converge at the detector in Fig. 1.17 after diffraction by the 2θ angle. Different detector positions provide different 2θ angles.

In the earliest days of the Debye–Scherrer technique, a stationary strip of photographic film was placed around the goniometer circle, eliminating the need for precise mechanical movements. This concept has been extended to digital data acquisition with wide angle position-sensitive detectors (PSD), which intercept an

Fig. 1.17 Geometry of the focusing circle



arc of 120° or so (see chapter title image). Instead of detecting in sequence x-rays diffracted into angular intervals of about 0.1° , diffractions over the full 120° angle are detected simultaneously by the PSD. The obvious advantage of these PSD diffractometers is their high rate of data acquisition, which may be hundreds of times greater than conventional powder diffractometers with goniometer movements.

1.3.3 Monochromators, Filters, Mirrors

Monochromatization of x-rays is best performed by Bragg diffraction from single crystals. A good monochromator can be built with a Johansson crystal (shown on its focusing circle in Fig. 1.17), together with slits located at the positions of the “tube” and the “detector.” This design makes efficient use of the divergent x-rays leaving the x-ray tube. The monochromated x-rays form a non-parallel, convergent beam, however, and a non-parallel beam can be a disadvantage for some applications. A more parallel monochromatic beam can be produced with an “asymmetrically cut” curved single crystal. The asymmetrically cut crystal has its crystal planes aligned with those shown at the top of Fig. 1.17, but its surface is cut asymmetrically with respect to the diffracting planes, as shown on the right side of Fig. 1.17. The asymmetrically-cut crystal intercepts a broad range of incident angles. Its surface is foreshortened as seen from the detector, however, so its diffracted beam is less convergent. Compression of the beam divergence by a factor of 10 is possible with such an asymmetrically-cut crystal.

Installing a monochromator in the diffracted beam at the position of the detector¹⁵ in Fig. 1.15 can improve the signal-to-background ratio of the diffraction pattern. Diffractions from incident bremsstrahlung and other contamination radiations from the x-ray tube are no longer detected, because these radiations have the wrong wavelength to pass through the diffracted beam monochromator. Likewise, there is no detection of fluorescence x-rays emitted by the sample when excited by the incident beam. Sample fluorescence is usually emitted in all directions in front of the specimen, contributing a broad background to the measured diffraction pattern. Sample fluorescence can cause a serious background problem when there are elements in the specimen having atomic numbers, Z , that are less than the atomic number of the anode material by 2 to 5, or when the energetic bremsstrahlung from the x-ray tube is sufficiently intense (as can occur when the anode is a heavy element). Installing a monochromator in the incident beam, rather than the diffracted beam, can eliminate problems from diffracted bremsstrahlung and other contamination radiations, but an incident beam monochromator cannot prevent the detection of fluorescence from the specimen.

In the incident beam it is sometimes useful to install a filter, typically a thin foil of absorbing material,¹⁶ for suppressing the $K\beta$ x-rays from the tube. If the foil is made from an element with an atomic number 1 less than that of the anode, the more energetic $K\beta$ x-rays are attenuated strongly because they cause the foil to fluoresce. The desired $K\alpha$ radiation does not induce fluorescence and is attenuated less. Finally, it should be noted that a detector with high energy resolution may not necessarily require a monochromator or filter, since discrimination of unwanted radiations can be accomplished electronically. Nevertheless, reducing the flux of unwanted radiations may improve the performance of the detector, especially at high count rates.

The focusing of x-rays by curved mirrors was proposed by Kirkpatrick and Baez in 1948, but “K–B mirrors” have become important recently owing to improved fabrication methods and brighter x-ray sources. The essential idea is that the index of refraction of x-rays in most materials is slightly less than 1, typically about 0.99999. If the incident angle of an x-ray from vacuum to the material is less than a critical angle, total reflection will occur. These critical angles are small, of order 1° , so the x-ray beam makes only a glancing angle to the surface of the mirror. This sets stringent requirements over a substantial length of the surface of the mirror. For x-ray beams of narrow divergence and small diameters, as are typical of synchrotron undulator beams, curved K–B mirrors are practical for focusing the beam. Often two pairs of mirrors are used, one for focusing horizontally and the other vertically, producing a spot of a micron or so at the focal point.

¹⁵More precisely, the point labeled “tube” in Fig. 1.17 is located at the center of the “receiving slit” of Fig. 1.15 (and the drawing of Fig. 1.17 is rotated 90° clockwise).

¹⁶The thickness of a filter can be calculated with the method of Sect. 4.2.3.

1.4 X-Ray Detectors for XRD and TEM

1.4.1 Detector Principles

An x-ray detector generates a pulse of current when it absorbs an x-ray. Several criteria are useful for characterizing its performance. First, the ideal detector should produce an output pulse for every incident x-ray. The fraction of photons that produce pulses is the “quantum efficiency” of the detector, QE . On the other hand, the detector and its electronics should not generate false pulses, or noise pulses. A “detective quantum efficiency” (DQE) combines the effects of quantum efficiency with signal-to-noise ratio (SNR) as a measure of how long different detectors (of the same geometry) must count to acquire data of the same statistical quality. The DQE is defined as square of the ratio of the SNR of the actual detector to the SNR of an ideal detector (where the SNR originates only with counting statistics):

$$DQE \equiv \left(\frac{SNR_{\text{actual}}}{SNR_{\text{ideal}}} \right)^2, \quad (1.37)$$

assuming the counting times for the actual and ideal detectors are equal.¹⁷

Second, the detector should produce a pulse of current having a net charge proportional to the energy of the x-ray photon. When detecting photons of the same energy, the voltage pulses from the electronics should all have the same height, or at least the distribution of pulse heights should be narrow. The width of this distribution for monochromatic x-rays is known as the detector energy resolution, usually expressed as a percentage of the x-ray energy. When acquiring a spectrum of characteristic x-rays, as in energy-dispersive spectrometry (EDS) in a TEM, energy resolution is a central concern. Energy resolution is less critical for x-ray diffractometry, but is still desirable because energy resolution allows the subsequent electronics to better discriminate against noise and unwanted radiations.

Third, the amplitude of the detector pulses should remain steady with time, and should not vary with the incident x-ray flux. If the amplitude of the output pulses decreases at high count rates, the energy spectrum is blurred. There is also an undesirable “dead time” after the detection of a photon before the detector is able to detect a second one. This dead time should be short. At high count rates, dead time can cause measured count rates to be sub-linear with the actual x-ray flux. (At extremely high fluxes, the count rate of some detectors can even fall to zero.)

Finally, for EDS spectrometry in a TEM, it is important to maximize the solid angle subtended by the detector from the specimen.

¹⁷Suppose a detector does not generate noise of its own, but its $QE = 1/2$. For the same x-ray flux as an ideal detector, this detector would have half the signal and half the noise, but $SNR_{\text{actual}}/SNR_{\text{ideal}}$ is not 1.0. With half the countrate, counting statistics reduce this ratio to $\sqrt{1/2}$. The DQE of (1.37) would then be $1/2$, so $DQE = QE$ for detectors that do not generate false counts.

Table 1.3 Features of x-ray detectors

Detector	Resolution at 10 keV	Count Rate	Comments
gas-filled proportional	Fair (15 %)	< 30 kHz	robust
scintillator	Poor (40 %)	Good ~ 100 kHz	robust
Si[Li]	Good (2 %)	Poor < 10 kHz	liquid nitrogen
intrinsic Ge	Good (2 %)	< 30 kHz	liquid nitrogen
silicon drift	Good (2 %)	200 kHz	–50 °C
wavelength dispersive	Excellent (0.1 %)	Good ~ 100 kHz	mechanically delicate narrow acceptance
calorimetric	Excellent (0.1 %)	Poor < 10 kHz	research stage
avalanche photodiode	Fair (20 %)	Excellent > 10 MHz	electrically delicate

Some characteristics of x-ray detectors are summarized in Table 1.3. All can have high quantum efficiency, depending on the x-ray energy and the detector material or geometry. The gas-filled proportional counter is the oldest and simplest. The gas in this detector is ionized when it absorbs the x-ray energy. The electrons are attracted to the anode wire, which is biased at a high positive voltage. In the strong electric field near the anode wire, these electrons build up enough kinetic energy in a mean free path so they ionize additional gas atoms, and more electrons are created in this process of “gas gain.” The gas-filled proportional counter is inexpensive and has modest energy resolution, but its gas gain decreases with count rate.

A scintillator is a piece of material, such as NaI made optically active by doping with Tl, that makes a brief flash of light when it absorbs an x-ray. The light is conducted to a photomultiplier tube, whose photocathode emits electrons when illuminated. The electron pulse is amplified further in the photomultiplier tube. Scintillation detectors are usable to very high count rates, but have poor energy resolution at typical x-ray energies. If energy resolution is not important, or if energy resolution is provided by a monochromator preceding the detector, a scintillation detector is often the best buy for a conventional x-ray diffractometer. The thickness of the scintillator should be sufficient to provide for strong absorption of the incident photon, and this thickness can be calculated from the mass-absorption coefficients discussed in Sect. 4.2.3. The required thickness of the active region of most other types of detectors can be obtained in a similar way.

A new type of x-ray detector is based on the calorimetric detection of x-ray energy. A superconducting wire held near its transition temperature is highly sensitive to small temperature excursions, and can be used to detect the heat energy deposited by an individual x-ray. The heat can be measured with sufficient accuracy to provide x-ray energy resolutions of 0.1 %, significantly better than solid state detectors. The limit on the energy resolution of such detectors is thermal noise, which can be suppressed by operating at temperatures below 0.1 K. Cryostats and cooling systems

based on adiabatic demagnetization have been developed that allow operation of high performance calorimetric detectors for tens of hours per cooldown. At present the thermal response times of the detectors are somewhat long, limiting their maximum count rate. To shorten thermal response times, smaller detector geometries are under development.

1.4.2 Solid State Detectors

Solid state detectors have good energy resolution, and can be designed to work as individual devices or arrays. They are silicon or germanium diodes, operated with reverse bias. Electrical contacts to the semiconductor surfaces are typically provided by thin layers of gold. Adjacent to the two contacts are *p*-type and *n*-type semiconductor, but most of the detector element is undoped, termed an “intrinsic” semiconductor. Commercial silicon typically has a residual *p*-impurity content that requires compensation with an *n*-type impurity. Lithium is typically used for this purpose, and such an intrinsic detector is called a Si[Li] detector. Other intrinsic detectors use pure Ge, and these can offer better performance.

An intrinsic semiconductor has no impurity levels in its band gap, so there is little thermally-activated current in reverse bias, especially when the detector is cooled with liquid nitrogen. An incident x-ray causes the excitation of electrons from the valence band into the conduction band, with an average energy per pair that is somewhat greater than the energy of the band gap. The high voltage of the reverse bias causes the electrons and holes to drift to their appropriate electrodes, providing a pulse of current through the diode. The total number of charge carriers is two times the energy of the x-ray photon divided by the average energy of the electron-hole pair. The net charge conducted across the diode is typically a few thousand electrons for typical x-ray energies. If the creation of each electron-hole pair required exactly the same energy, there would be a precise relationship between the x-ray energy and the current pulse, so the detector would have superb energy resolution. There is a statistical distribution of the electron-hole creation energies, however, causing differences in the number of electron-hole pairs generated by identical x-rays. When monochromatic x-rays each generate thousands of electron-hole pairs, the energy resolution is typically about 2 %. The energy resolution of a solid state detector remains good so long as the count rate is not excessive, so there is no interaction between charge carriers generated by different x-rays.

Solid state detectors cause some spectral distortions and artifacts. When the primary ionization event occurs in the inactive “dead” layer near the contacts to the diode, not all the charge is collected. This causes the appearance of a low-energy tail on a spectrum from monochromatic radiation. Finally, the silicon itself can be ionized, with a threshold of 1.74 keV. If a silicon atom deep within the diode is ionized, most of this energy is eventually converted into electron-hole pairs and this presents no problem. However, if a silicon atom near the edge of the detector is ionized, this 1.74 keV energy may escape from the detector. Secondary “escape peaks”

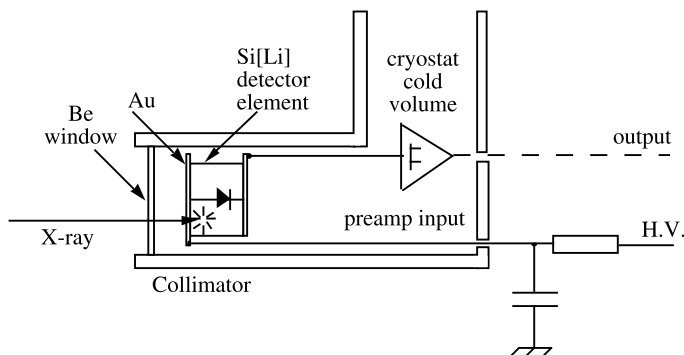


Fig. 1.18 Experimental configuration for a solid state detector. The cold volume of the cryostat is typically near the temperature of liquid nitrogen

therefore appear in the energy spectrum from a Si[Li] detector. These escape peaks are located consistently at energies 1.74 keV below the energies of the main peaks in the spectrum.

A typical experimental configuration for a solid state detector is presented in Fig. 1.18. To minimize thermal noise from the diode and from the preamplifier electronics, and to prevent damage to Si[Li] detectors by diffusion of Li during reverse bias, the detector is typically cooled with liquid nitrogen. The detector must then be kept in vacuum to prevent ice and hydrocarbon condensation on its surfaces. A beryllium window typically provides vacuum isolation for the detector, and this window must have sufficient thickness to withstand a pressure differential of 1 atmosphere. Unfortunately the beryllium window, the gold layer on the semiconductor, and the inactive (“dead”) layer of silicon near the gold contacts all attenuate the incident x-rays. This attenuation is particularly significant for x-rays with energies below 1 keV. The beryllium window confines energy-dispersive spectrometry (EDS) to the identification of elements of atomic number $Z = 11$ (sodium) or larger. Even for “ultrathin window EDS,” where polymeric films are employed, or “windowless EDS” where the detector and specimen share the same vacuum space, it is typically impractical to detect elements lighter than boron ($Z = 5$). As discussed in Sect. 5.6.2, the fluorescence yield of x-rays becomes very small for the lightest elements—excited states in these atoms usually decay by Auger electron emission.

A silicon drift detector (SDD) is a new type of solid state x-ray detector that is starting to see widespread service in energy dispersive spectroscopy. The detector is shaped as a thin disk of perhaps 300 μm thickness and 1 cm diameter, with its electron collector in the center of a flat surface. On the surface around the electron collector is a pattern of ring-shaped anodes that control the potential inside the disk, guiding the electron drift to the central current collector. The drift time is predictable, and more than one electron bunch at a time can be in transit to the electron collector. The field effect transistor at the preamplifier input can be integrated into the detector itself, further reducing capacitance. Some advantages of the SDD over a Si[Li] detector is its large area, high count rate owing to low capacitance (sub-pF),

and the requirement for only modest cooling, typically provided by a Peltier cooling system.

An x-ray spectrometer is an integral part of an analytical transmission electron microscope. The vast majority of x-ray spectrometers in analytical TEM use solid state detectors, positioned with a direct view of the specimen. Today SDD detectors are rapidly replacing the Si[Li] detectors that have been used for decades. The energy resolution of an EDS spectrometer can lead to challenges when several elements are present in a sample. When characteristic energies are close together, peaks from individual energies may not be resolved. Such overlaps are common for the *L* and *M* lines of medium- and high-*Z* elements, respectively. It is a task of the spectrometer software to help untangle spectra with multiple peak overlaps, usually by fitting the measured spectrum to patterns of peaks from each element.

1.4.3 Position-Sensitive Detectors

High performance x-ray diffractometers have been built around position-sensitive detectors (PSD). Since a PSD detects x-rays at many angles simultaneously, it can minimize data acquisition times and improve counting statistics. There are many designs for PSDs, and all have unique features.

Several types of PSDs are gas-filled counters. One design uses a resistive wire as an anode, and a preamplifier at each end of the anode wire. The position of the x-ray is determined by the difference in charge detected by the two preamplifiers. An x-ray that ionizes the gas at one end of the detector tube produces a larger pulse in the preamplifier connected to that end. Such detectors require that the resistivity of the anode wire be steady with time, and not affected by contamination from the detector gas, for example.

A second type of gas-filled PSD makes use of time delays along electrical transmission lines. For example, the cathode surface may be subdivided into hundreds of independent plates, each connected to its neighbor by a small inductor and capacitor. Preamplifiers are located at each end of the cathode chain, and the time difference between their two signals is measured. The position of the x-ray is closer to the preamplifier that produces the earlier pulse. The same time-delay concept is used in a design for a two-dimensional area detector. This detector uses crossed grids of anode wires, with wires running in the *x*-direction providing information on the *y*-coordinate of the event, and the wires running in the *y*-direction providing information on the *x*-coordinate. The individual wires in each anode grid are connected to their neighbors by an inductor and capacitor, providing a delay time along the grid. The electronics for these area detectors are complex and must be considered an integral part of the detector system. Gas-filled delay-line counters have low noise, but usually no energy resolution.

Another type of area detector is based on a video camera system using charge-coupled-devices (CCDs). The CCD chips themselves serve as excellent, small x-ray detectors (assuming their active regions are sufficiently thick to stop the x-rays).

They suffer radiation damage after a large number of detected x-rays, but are well-suited for low flux experiments. To reduce radiation damage, a thin scintillator can be used to stop the x-rays. The light from the scintillator enters the CCD by direct contact, or by focusing the light from a large scintillator onto the CCD through a lens or a tapered bundle of optical fibers. At low x-ray fluxes, thermal and readout noise may be a consideration for CCD area detectors, but a CCD area detector could have energy resolution at low x-ray fluxes when individual events are identified.

Developments in semiconductor processing technologies have made possible a number of new types of PSDs based on silicon diodes or diodes of other semiconductor materials such as CdTe. Typically an array of square diode detectors is arranged over the surface of a large semiconductor chip. Each diode requires its own preamplifier and pulse processor electronics, and these are typically provided by a customized analog integrated circuit. Further electronic integration can include a multichannel analyzer (see next section), but this is typically shared (multiplexed) by a number of diodes, and can limit the peak rate of data acquisition. Pixelated diode PSD systems can provide full digital output, such as an alert to a detected event, followed by the pixel identification number and a number proportional to the energy of the event.

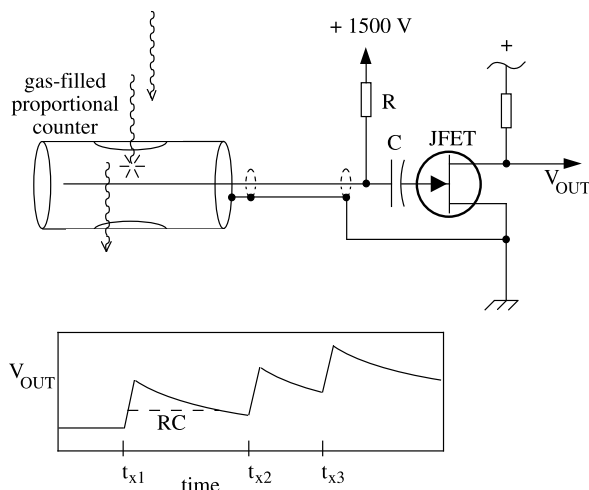
The large and competitive marketplace for medical x-ray imaging equipment is spawning a number of developments in area detectors. Imaging plates, for example, are relatively inexpensive, and are handled in much the same way as photographic film. The plates include a layer of long-persistence phosphor, BaFI with Eu ions, for example. The x-ray excites the Eu^{2+} to Eu^{3+} , which persists for a day or so. The locations of the Eu^{3+} (the locations of the x-ray detections) are found by transporting the imaging plate to a readout unit, where a He–Ne laser beam is rastered over the entire plate. The Eu^{3+} is identified by its photostimulated blue light. The imaging plates themselves are later erased and reused. Unlike photographic film, the signal from imaging plates is linear over 6 or more decades, and the sensitivity to low exposures of x-rays (and electrons) is excellent. Energy resolution is usually impractical.

Although PSDs usually provide enormous improvements in data acquisition times (factors of 10^3 are possible), they have some limitations. Besides their higher cost, they have a reputation for requiring skill to operate and maintain. Several newer designs are robust and convenient, however. Most gas-filled PSDs do not provide energy resolution. This can be a problem in the presence of strong sample fluorescence as discussed in Sect. 1.3.3.

1.4.4 Charge Sensitive Preamplifier

Typical charge sensitive preamplifiers have input circuits like the one in Fig. 1.19, shown with a gas-filled proportional counter. The capacitor, C , integrates the negative charge collected on the anode wire, causing a quick rise in resistance across the field effect transistor. A small value of C allows for a large rise in voltage and good

Fig. 1.19 Input circuit for a simple charge sensitive preamplifier, here operating with a gas-filled proportional counter. The time-dependent voltage across the field effect transistor (FET) is indicated schematically after detection of an x-ray at times t_{x1} , t_{x2} , and t_{x3}



sensitivity. On the other hand, small stray capacitances between the detector and the preamplifier can have a detrimental effect on the detector signal, so interconnections between detector and preamplifier are kept as short as possible. The resistor, R , bleeds away the voltage across C with a much longer time constant. Typically, $RC = (10^7 \Omega)(10^{-11} \text{F}) = 10^{-4} \text{ s}$. A preamplifier with higher performance for solid state detectors is constructed with the detector output sent directly into an FET operational amplifier (cf., Fig. 1.18). This op-amp is configured as an integrator by using a capacitor in its feedback loop. The discharge of this capacitor is provided by a fixed resistance across it, or by an active circuit that discharges the capacitor when the integrated voltage exceeds a setpoint.

1.4.5 Other Electronics

A full system for x-ray detection and spectroscopy is shown in Fig. 1.20. Following the preamplifier is a main amplifier. Its primary purpose is to shape the pulses into a convenient waveform, such as a Gaussian function with a width of a few microseconds, all the while ensuring that the height of the pulse remains proportional to the charge collected on the capacitor of the preamplifier. An important function of the main amplifier is to compensate for the slow decay set by RC of the preamplifier. This exponential decay is quite predictable. The main amplifier compensates for this decay in a process called “pole-zero” cancellation, which provides a flat voltage baseline following each sharp Gaussian pulse. The main amplifier may not separate two pulses from the preamplifier that arrive closely in time, causing an artifact where the two closely-spaced pulses are shaped into one large pulse. These large pulses appear in an x-ray spectrum at the sum of the energies of the real peaks, and this artifact is called a “sum peak.” The fraction of sum peaks becomes larger at high counting rates.

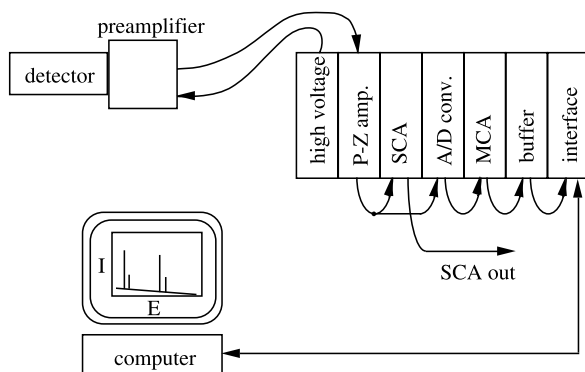


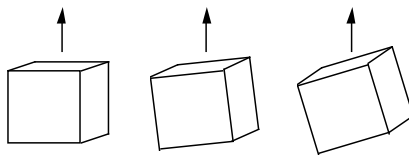
Fig. 1.20 Full x-ray spectroscopy system. The interface unit allows the computer to download the spectra, and allows the computer to control the electronic units. For an analytical TEM, the SCA output may be directed to a STEM unit for elemental mapping. An x-ray diffractometer may have the SCA output sent to a simple counter, and the subsequent electronic units such as the MCA may be needed only for calibration and diagnostic work

For x-ray diffractometry, there are many small pulses coming out of the main amplifier that are low amplitude noise, or unwanted pulses from undesired types of radiations such as sample fluorescence. It is the job of the single channel analyzer (SCA, or “window discriminator”) to set upper and lower thresholds to define the pulses of interest. The counts from the SCA are accumulated in a counter or in a memory bin assigned to a particular 2θ angle of the goniometer. A computer system is typically used to synchronize the stepper motors in the goniometer with the memory bin used for data acquisition. Besides its data acquisition and control functions, the computer also is often used for data display, storage, processing, and transmission to other computers.

For analytical TEM, a solid state detector is used for the collection of the full spectrum of x-ray energies. For most work in analytical TEM, an energy spectrum is acquired by sending the shaped pulses from the main amplifier into a multichannel analyzer, or MCA. In the MCA, the pulse is first converted into a digital number by a fast analog-to-digital converter. A single count is added to the content of the MCA memory address corresponding to that number. With time, a histogram is collected in the memory of the MCA, displayed as the number of counts versus memory address. With an energy calibration provided by a source of known monochromatic photons,¹⁸ the (linear) correspondence between the memory address and the photon energy can be determined. This histogram can then be displayed as an x-ray energy spectrum. When performing elemental mapping, the SCA registers counts from a selected x-ray energy, and this SCA output is an input signal to the STEM raster display in Fig. 2.1.

¹⁸Such as a radioisotope source or a known atomic fluorescence.

Fig. 1.21 Various orientations of crystallites with respect to the best orientation for diffraction



1.5 Experimental X-Ray Powder Diffraction Data

1.5.1 * *Intensities of Powder Diffraction Peaks*¹⁹

Which crystals contribute to the Bragg peaks in a powder diffraction pattern? If nature demanded that diffracting crystallites were in exact Bragg orientations, then a powder containing a finite number of crystals would have zero crystallites that diffract. We observe diffractions with monochromatic radiation, so evidently the crystals need not be oriented perfectly. This is especially true if they are small and have broadened diffractions.

In this section we consider the numbers of crystallites that are oriented “adequately” for diffraction. Three types of crystal orientations are shown in Fig. 1.21. Assume that the crystal at the left is oriented perfectly. It diffracts strongly, but there are very few such crystals. The one in the middle is misoriented a little. It does not diffract so strongly, but there are more such crystals. There are even more crystallites with the large misorientation of the right cube, but these crystallites contribute little to the diffracted intensity because they are far from the Bragg orientation. In powder diffraction we measure the number of crystallites that are within some small range of misorientations.

The intensity of a powder pattern diffraction peak is controlled in part by geometrical aspects of the diffractometer and the sample. It is not our intent to calculate the absolute intensity of a powder diffraction peak because most x-ray diffractometry studies on materials are performed in a comparative way where absolute intensity is unimportant. It is instead important to know the systematic trend of how the intensities of the different (hkl) diffractions depend on the 2θ angle of the diffractometer. We consider individual effects as intensity correction factors, and present two examples of total correction factors in (1.54) and (1.55).

1.5.2 *Normals of Diffracting Planes*

Consider Fig. 1.22, where the incident and outgoing arrows make angles, θ , with the plane of the specimen. For a specific angle, θ , we want to know how many crystal-

¹⁹Throughout this book, an asterisk (*) in a section heading denotes a more specialized topic. For example, the results of the present section, (1.54) and (1.55), are important, but on a first reading the reader may choose to avoid the details of their derivation. Incidentally, a section heading with a double dagger (‡) indicates a higher level of mathematics.

Fig. 1.22 Band of projected normals of crystallite planes capable of diffraction

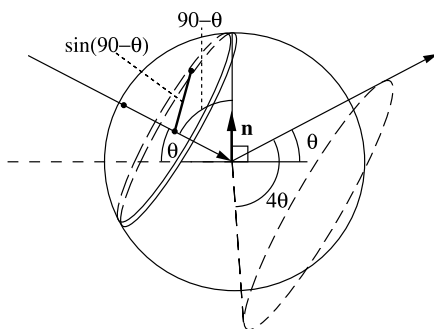
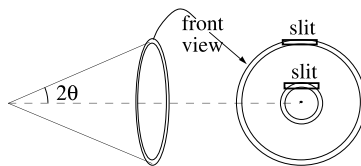


Fig. 1.23 Interception of the diffraction cone by the detector slit



lites are oriented within an angular range suitable for diffracting into the diffraction cones of Fig. 1.8. The normals to these crystallites point to the ring drawn around the sphere in Fig. 1.22. Assuming the orientations of the crystallites are isotropic, we see that the number of these crystallites, and the diffracted intensity, is proportional to:

$$I_1 \propto \sin(90 - \theta) = \cos \theta. \quad (1.38)$$

1.5.3 Slit Width

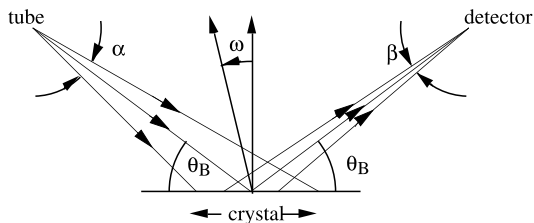
Not all of the x-rays diffracted into the ring in Fig. 1.22 are seen by the detector. The detector has a receiving slit with a limited horizontal width, as shown in Fig. 1.23. Owing to the horizontal width of its receiving slit, the detector collects a larger fraction of x-rays from diffraction cones of smaller 2θ . The fraction detected is proportional to:

$$I_2 \propto \frac{1}{\sin(2\theta)}. \quad (1.39)$$

1.5.4 Lorentz Factor

A crystallite can diffract even if it is not oriented at an exact Bragg angle. Small deviations from the Bragg angle are acceptable, provided the path length differences of the rays remain close to an integral number of wavelengths. The “Lorentz factor” is product of geometrical factors that account for the number of crystallites that

Fig. 1.24 Misorientation angles of a powder diffractometer



can diffract, given some angular divergence of the incident and diffracted beams, and a distribution of normals of the Bragg planes. The Lorentz factor modifies the intensities of diffraction peaks across a broad range of 2θ as in Fig. 1.2. Figure 1.24 depicts an imperfect diffraction experiment with a crystallite misoriented from its proper Bragg angle by the amount ω , an incident beam with a divergence angle, α , and a receiving slit to intercept diffractions within the angle β . We obtain the Lorentz Factor by calculating the effects of nonzero α , β , and ω on the path length differences of two rays scattered from different planes in the crystal, starting with a condition where the two path lengths differ precisely by an integral number of x-ray wavelengths when α , β , and ω are zero. We seek the θ -dependence of the peak intensities. We use bounds on the path length differences to provide bounds on the allowable ranges of θ , treating the $\{\alpha, \beta\}$ and ω dependencies separately as the “acceptable divergence factor” of the instrument, and as the “tilt sensitivity factor” of the crystal.

Acceptable Divergence Factor To obtain the “acceptable divergence factor,” we ignore the crystal tilt (set $\omega = 0$). Consider the path length error for a ray that enters and/or leaves the crystallite at an angle, $\theta = \theta_B + \Delta\theta$, slightly different from the Bragg angle. (Consider Fig. 1.1 with a tilted incident beam.) Between any two diffracting planes separated by d , the path length is not λ as in (1.1), but rather $\lambda + \delta l$:

$$\lambda + \delta l = 2d \sin(\theta_B + \Delta\theta). \quad (1.40)$$

We seek the sensitivity of the path length change, δl , to variations in θ -angle caused by beam divergence. We start by differentiating (1.40):

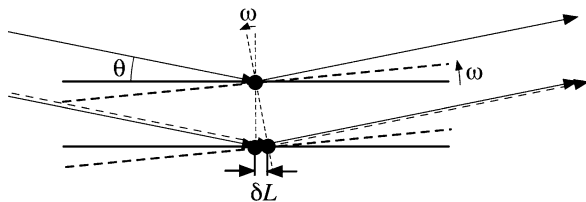
$$\frac{d}{d\theta}[\lambda + \delta l] = \frac{d}{d\theta} 2d \sin(\theta_B + \Delta\theta)|_{\theta=\theta_B}, \quad (1.41)$$

$$\frac{d\delta l}{d\theta} = 2d \cos \theta. \quad (1.42)$$

Equation (1.42) shows that the path length error depends on the angular divergence as $\cos\theta$. As the diffraction angle approaches 90° , large errors in incident angle cause only small path length errors,²⁰ so a greater number of incident rays can undergo

²⁰Equation (1.42) implies that for an instrument with fixed divergences, crystal plane spacings are best determined from peaks at the largest diffraction angles (see also Sect. 1.5.13).

Fig. 1.25 Effects of sample tilt, ω , on path length differences for x-rays scattered from two planes, drawn for a small incident angle, θ



diffraction. The same argument is valid for either the incident or the diffracted beam, but the effective divergence is set by the narrowest of either of them. The intensity therefore varies as:

$$I_3 \propto \frac{1}{\cos \theta}. \quad (1.43)$$

Tilt Sensitivity Factors To obtain the “tilt sensitivity factors,” we ignore the divergence of the incident and diffracted rays (set $\alpha = \beta = 0$). In other words, we fix the 2θ angle, but tilt the crystal so that the incident and outgoing θ are not equal. This tilt causes destructive interference, as shown in Fig. 1.6, but crystallites within some range of misorientations (within a range in the angle ω of Fig. 1.24) can still contribute to the signal at the detector. We are not concerned with the actual range of ω , but we obtain the θ -dependence of this tilt sensitivity by analyzing the total phase shift of the incident and diffracted rays.

Section 1.1.5 explained how a tilt of crystallographic planes (parameterized by how the plane normals, \mathbf{n} , were misdirected from the diffraction vector $\Delta\mathbf{k} \equiv \mathbf{k} - \mathbf{k}_0$) caused inconsistent path lengths for rays scattered from points O and P on the diffracting plane in Fig. 1.6. For the interference of waves scattered from atoms on different planes, Fig. 1.25 shows that the path length error is much less sensitive to crystal tilt, ω , if the incident angle is low (i.e., θ is small). In fact, as $\theta \rightarrow 0$, Fig. 1.25 shows how the incident path to the bottom plane increases by δL , whereas the outgoing path decreases by δL , leaving the total ray path unchanged.²¹ This error in path length increases as $\sin \theta$, so the intensity factor, I_4 , has the θ -dependence:

$$I_4 \propto \frac{1}{\sin \theta}. \quad (1.44)$$

Wavelength Another way of getting more constructive interference from a crystal is to simply reduce its interplanar spacing. For a fixed number of diffracting planes, errors in orientation are less detrimental to constructive interference when the planes are closer together, because the x-ray path length differences between the top and bottom planes are smaller. The same effect can be obtained by increasing the wavelength of the x-rays, since phase differences over a fixed path length are smaller for x-rays of longer wavelength. These same arguments (cf., Sect. 1.1.3)

²¹Even for amorphous solids, diffraction is coherent in the forward direction, for which $\theta = 0$.

apply to errors in orientation along each dimension of the diffracting plane, so the diffraction intensity scales as:

$$I_5 = \frac{\lambda^3}{V_c}, \quad (1.45)$$

where V_c is the volume of the unit cell of the crystal.

All the intensity factors, I_3 , I_4 , and I_5 , act independently. The Lorentz factor, $I_{3,4,5}$, is the product of (1.43), (1.44), and (1.45):

$$I_{3,4,5} \propto \frac{\lambda^3}{V_c} \frac{1}{\cos \theta \sin \theta}, \quad (1.46)$$

$$I_{3,4,5} \propto \frac{\lambda^3}{V_c \sin 2\theta}. \quad (1.47)$$

1.5.5 Absorption

X-rays are absorbed individually as they pass through a specimen, and the number of them decreases as $e^{-\mu \varrho x}$, where x [cm] is the distance traveled through the material, μ [cm²/g] is the mass absorption coefficient, and ϱ [g/cm³] is the density of the material (see Sect. 4.2.3). The intensity of a diffraction peak is proportional to the average number of x-rays that reach each volume of material, and then successfully leave the specimen. For some experimental geometries, the ratio of absorption to diffraction varies with diffraction angle, altering the relative intensities of the Bragg peaks. Fortunately this is not so for a thick, flat polycrystalline specimen when the incident and diffracted angles, θ , are the same (see Problem 1.5). With a shallower diffraction angle, θ , the x-rays do not penetrate so deeply into the sample, but the specimen is illuminated across a larger width. For thick, flat specimens there is no net angular dependence for the absorption correction. Samples with larger absorption coefficients, μ , do not permit deep x-ray penetration, so the intensity factor is proportional to $(\mu \varrho)^{-1}$:

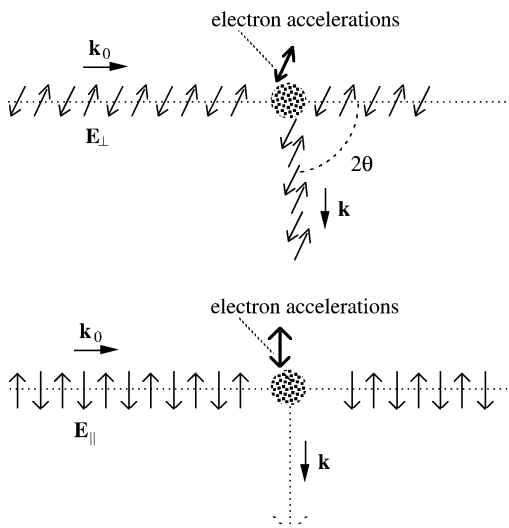
$$I_6 \propto \frac{1}{\mu \varrho}. \quad (1.48)$$

This argument is not valid if the incident and diffracted angles are different. Consider, for example, a diffraction measurement on a flat specimen with a position sensitive detector using a fixed incident angle. The penetration of the incident beam is the same for all 2θ , but the absorption of the scattered x-rays varies with 2θ . The intensity correction is:

$$I_{6\text{psd}} \propto \frac{1}{\mu \varrho} \frac{\sin \zeta}{\sin \phi + \cos \zeta}, \quad (1.49)$$

where ϕ is the angle of incidence with respect to the plane of the specimen, and ζ is the exit angle ($2\theta = \phi + \zeta$).

Fig. 1.26 Scattering at 90° angles is affected strongly by the polarization of the incident wave. In the *lower drawing* there is no scattering at $2\theta = 90^\circ$ because \mathbf{E} would be parallel to \mathbf{k}



1.5.6 Polarization

Section 4.2.1 describes how the electric field of the x-ray photon causes the atomic electrons to oscillate. The accelerations of these electrons cause the re-radiation of the scattered wave. Consider a back-and-forth oscillation that creates dipole radiation. In the top drawing of Fig. 1.26, the electric field, \mathbf{E}_\perp , of the incident x-ray is polarized out of the plane of the paper; in the bottom drawing \mathbf{E}_\parallel is polarized in the plane of the paper. It is possible to scatter the x-ray in the top drawing over a 90° angle in the plane of the paper, but this is not so for the x-ray in the bottom drawing because the electron accelerations would be parallel to the outgoing wavevector. The scattered x-ray would have an electric field parallel to its wavevector, which is impossible. For these two polarizations of incident x-radiation, the wave amplitude for the top drawing is independent of scattering angle, whereas the wave amplitude for the bottom case is proportional to $\cos 2\theta$, where 2θ is the scattering angle. For an unpolarized incident x-ray beam, the scattered intensity depends on scattering angle as:

$$I_7(\theta) = |\mathbf{E}|^2 = |\mathbf{E}_\perp|^2 + |\mathbf{E}_\parallel|^2 \propto \frac{1 + \cos^2 2\theta}{2}. \quad (1.50)$$

1.5.7 Multiplicity and Density

Different crystallographic planes have different “multiplicities” or variants. For example, the $\{200\}$ planes have six variants, $\{(200), (\bar{2}00), (020), (0\bar{2}0), (002), (00\bar{2})\}$,

whereas the $\{110\}$ planes have twelve. In a powder without texture, an incident x-ray is twice as likely to encounter a properly-oriented $\{110\}$ plane than a $\{200\}$ plane. This multiplicity of diffracting planes multiplies the intensity of the diffraction peak by m , where $m = 12$ for a $\{110\}$ diffraction and $m = 6$ for a $\{200\}$ diffraction.

The number of diffracting atoms per unit volume is inversely proportional to the volume of the unit cell, V_c , so a given volume of material with smaller unit cells diffracts more strongly. Together the multiplicity and density provide an intensity factor:

$$I_8 \propto \frac{m}{V_c}. \quad (1.51)$$

1.5.8 Measured Intensities

Putting together the results of this Sect. 1.5.2 for a flat crystal in a Bragg–Brentano diffractometer, the measured intensity of a diffraction from a flat specimen of polycrystalline powder is proportional to:

$$I(\theta) \propto I_1 I_2 I_{3,4,5} I_6 I_7 I_8, \quad (1.52)$$

$$I(\theta) \propto \frac{m\lambda^3 \mathcal{F}^*(\Delta k) \mathcal{F}(\Delta k)}{V_c^2 \mu_Q} \cos \theta \frac{1 + \cos^2 2\theta}{\sin^2 2\theta}, \quad (1.53)$$

$$I(\theta) \propto \frac{m\lambda^3 \mathcal{F}^*(\Delta k) \mathcal{F}(\Delta k)}{V_c^2 \mu_Q} \frac{1 + \cos^2 2\theta}{\sin \theta \sin 2\theta}. \quad (1.54)$$

The factor $(1 + \cos^2 2\theta)$ in (1.54) (and (1.55) below) must be changed if the incident beam were polarized from an incident beam monochromator or a synchrotron source. For a position-sensitive detector (PSD) with a fixed incidence angle, ϕ , and outgoing angle $\zeta \equiv 2\theta - \phi$, the measured intensity of a diffraction is proportional to:

$$I(\theta) \propto \frac{m\lambda^3 \mathcal{F}^*(\Delta k) \mathcal{F}(\Delta k)}{V_c^2 \mu_Q} \frac{1 + \cos^2 2\theta}{\sin \theta \sin 2\theta} \frac{\sin \zeta}{\sin \phi + \sin \zeta}. \quad (1.55)$$

Equations (1.53)–(1.55) include a new factor, the structure factor for the unit cell, $\mathcal{F}(\Delta k)$. It is discussed at length in Chap. 6. The structure factor describes how strongly a unit cell diffracts an x-ray in various directions. $\mathcal{F}(\Delta k)$ is approximately proportional to the number of electrons of the unit cell times an angular factor originating with the size and shape of the atom. It also depends on the symmetry of the unit cell as described in Sect. 6.3. When using (1.55) or (1.54) it is important to use the same unit cell for both $\mathcal{F}(\Delta k)$ and V_c .

1.5.9 Phase Fraction Measurement

X-ray diffraction procedures for phase quantification have been developed extensively for some specific materials, and the scientific literature includes many procedures for data analysis. For a few materials, the National Institute of Standards and Technology in the USA (NIST) sells Standard Reference Materials (SRM) with known phase fractions [1.6]. When quantitative phase fraction measurements are needed, checks with these standards are strongly encouraged. Even when quantifying phases in materials for which no NIST SRM samples are available, other SRM standards can help check the reliability of the equipment and data analysis. Some aspects of phase quantification are presented here.

1.5.10 Peak Ratio Method

Here is a hypothetical example of using (1.54) or (1.55) for determining the volume fractions of phases in a sample. Suppose we have a mixture of pure bcc Fe and pure fcc Al, and we seek x_{Al} and x_{Fe} , the volume fractions of Fe and Al in the mixture. We use a Bragg–Brentano diffractometer with Mo $K\alpha$ radiation. For good quantitative measurements we must take care of some experimental details. The samples²² should be smooth, thick and flat, or the absorption correction factor of (1.48) may be incorrect. Another important experimental concern is getting a good sampling of all crystal orientations. A few large individual crystallites can bias strongly the measurement of peak intensity, so fine powders are preferred. Experimental averaging over the crystallites is aided by rotating the sample around the ϕ -axis during data acquisition (Fig. 1.15), and perhaps by also rocking slightly the sample around an ω -axis. In quantitative analysis it is also important to ensure that the maximum countrate is well within the capability of the detector system, so the most intense diffraction peaks are not suppressed by countrate nonlinearities.

If bcc Fe and fcc Al are the only two phases present,²³ it is sufficient to find the ratio of the phase fractions, x_{Al} and x_{Fe} , since $x_{\text{Al}} + x_{\text{Fe}} = 1$. Suppose we have measured the integrated intensity (peak area minus background) of the (111) diffraction from the Al, $I_{111\text{Al}}$, and the integrated intensity (110) diffraction from the Fe, $I_{110\text{Fe}}$, and suppose for the sake of argument that we found them to be exactly equal. Although the ratio of peak intensities is 1.0, the ratio of Al to Fe in the sample is not 1.0. We need to normalize the (111)Al and (110)Fe intensities by (1.54):

$$\frac{x_{\text{Fe}}}{x_{\text{Al}}} = \left(\frac{8|\mathcal{F}_{\text{Al}}|^2 V_{\text{cFe}}^2}{12|\mathcal{F}_{\text{Fe}}|^2 V_{\text{cAl}}^2} \frac{1 + \cos^2 2\theta_{\text{Al}}}{\sin \theta_{\text{Al}} \sin 2\theta_{\text{Al}}} \frac{\sin \theta_{\text{Fe}} \sin 2\theta_{\text{Fe}}}{1 + \cos^2 2\theta_{\text{Fe}}} \right) \frac{I_{110\text{Fe}}}{I_{111\text{Al}}}. \quad (1.56)$$

²²It is a good idea to measure diffraction patterns from at least two samples, each one prepared and mounted independently.

²³A mixture of three or more unknown phases is still amenable to analysis by the ratio method, since another peak ratio equation is provided for each additional unknown.

From Bragg's law we find that the Al (111) diffraction is at $\theta = 8.75^\circ$, and the Fe (110) diffraction is at $\theta = 10.1^\circ$. For Mo $K\alpha$ radiation, the atom scattering factors, f , for Fe and Al are tabulated in Appendix A.3, and to get a structure factor for the unit cell, \mathcal{F} , these numbers should be multiplied by the number of atoms per unit cell, $\mathcal{F}_{\text{fccAl}} = 9.1 \times 4$ and $\mathcal{F}_{\text{bccFe}} = 18.9 \times 2$. The absorption coefficients are neglected, but with the risks described in the next subsection. Evaluating (1.56):

$$\frac{x_{\text{Fe}}}{x_{\text{Al}}} = 0.29, \quad (1.57)$$

$$\frac{x_{\text{Fe}}}{1 - x_{\text{Fe}}} = 0.29, \quad (1.58)$$

$$x_{\text{Fe}} = 0.225. \quad (1.59)$$

It may seem surprising that the concentration of Fe is so low, given the observation that the intensity of the (110)Fe peak is equal to the intensity of the (111)Al peak. The main reason for this discrepancy is that the scattering factor of an Fe atom is much larger than that of Al. An approximation to the correction factor on the right side of (1.56) is simply the square of the ratio of the atomic numbers of the elements. For this example with $I_{110\text{Fe}} = I_{111\text{Al}}$:

$$\frac{x_{\text{Fe}}}{x_{\text{Al}}} \simeq \left(\frac{13}{26} \right)^2 = 0.25. \quad (1.60)$$

In this brief analysis we assumed unpolarized incident radiation. We have also neglected the effects of temperature on the diffraction intensities. Since Fe and Al have similar Debye temperatures, which are relatively high, we do not expect temperature to affect strongly these low angle diffraction peaks in x-ray measurements performed at room temperature (see Sect. 10.2.2).

1.5.11 Absorption Factors

In obtaining (1.56), it looks wrong to assume the same absorption factors, $\mu_{\text{Fe}}Q_{\text{Fe}} = \mu_{\text{Al}}Q_{\text{Al}}$, because this present equation is incorrect. The situation is more subtle than this, however, and the assumption of equal absorption factors can be justified in two cases. Clearly if the chemical compositions and densities of the two phases are nearly the same, the absorption factor should be the same.

The second case where it is appropriate to equate the absorption factors is when the sizes of the particles of all phases are small compared to the x-ray penetration depth. When the matrix can be assumed to be a (non-granular) continuum, diffractions from aluminum and iron crystallites are subject to the same absorption factors. For our case of iron and aluminum, the inverse absorption length of the continuum, $\overline{\mu Q}$, depends on the phase fractions of Fe and Al, x_{Al} and x_{Fe} , as:

$$\overline{\mu Q} = x_{\text{Al}}\mu_{\text{Al}}Q_{\text{Al}} + x_{\text{Fe}}\mu_{\text{Fe}}Q_{\text{Fe}}, \quad (1.61)$$

or in general for N phases,

$$\overline{\mu_Q} = \sum_{j=1}^N x_j \mu_j Q_j. \quad (1.62)$$

Since x_{Al} and x_{Fe} are the unknowns in our quantification procedure, we must make some reasonable guesses of their values (perhaps we know the chemical composition of the material), or be conservative and assume that $\overline{\mu_Q}$ is set by the stronger x-ray absorber. For our example of bcc Fe and fcc Al with Mo $K\alpha$ radiation, from Table A.1 we find that $\mu_{\text{Fe}Q\text{Fe}} = 296 \text{ cm}^{-1}$ and $\mu_{\text{Al}Q\text{Al}} = 14 \text{ cm}^{-1}$. Absorption by the aluminum is negligible unless $x_{\text{Al}} > 0.9$. Assuming $x_{\text{Fe}} = 0.225$, the inverse absorption length of our continuum is approximated as $\overline{\mu_Q} = 0.225\mu_{\text{Fe}Q\text{Fe}} = 67 \text{ cm}^{-1}$. This gives a characteristic absorption length of 0.015 cm, or 150 μm . If our Fe and Al particles are smaller than 15 μm or so, the neglect of the absorption factor in (1.56) should be acceptable. Incidentally, had we used the less penetrating Cu $K\alpha$ radiation for this diffraction measurement, the particle sizes would have to be on the order of a 1 μm or less for quantitative analysis. This is one disadvantage of using Cu $K\alpha$ radiation for phase analysis of iron alloys. An ameliorating circumstance, however, occurs when the phases have values of $\mu_j Q_j$ that are not very different. In the limit as the absorption lengths of the phases become equal, it becomes acceptable to have the particle size larger than the mean absorption length (but then it must be true that the surface of the sample provides a representative sampling of the constituent phases in the bulk).

Equation (1.56) does not require that we relate the intensities of the diffraction peaks to absolute intensities of a standard sample, so this approach is sometimes called the “internal standard method.” It is possible in principle to measure only the intensity of the (111)Al diffraction, and estimate the fraction of Al by comparison with a standard sample of Al. The absorption correction is a serious problem in such a quantification procedure. As we just saw, the presence of Fe in the sample attenuates strongly the Al diffraction pattern. Without making large corrections for this effect, serious errors occur in any determination of x_{Al} from the intensity of the (111)Al diffraction alone.

1.5.12 Example: Retained Austenite in Steels

Here is a procedure for measuring small amounts of fcc “austenite” phase in bcc (sometimes nearly bcc) “martensitic” steels. NIST SRM samples with well-characterized amounts of austenite are available for checking the results. Retained austenite (γ -phase) is typically of similar chemical composition to the martensite (α' -phase), and of similar density. The top part of Fig. 1.27 is an x-ray diffraction pattern from a “9Ni” steel with some austenite. One of the authors has had success with the following semi-empirical relationship for determining the austenite volume

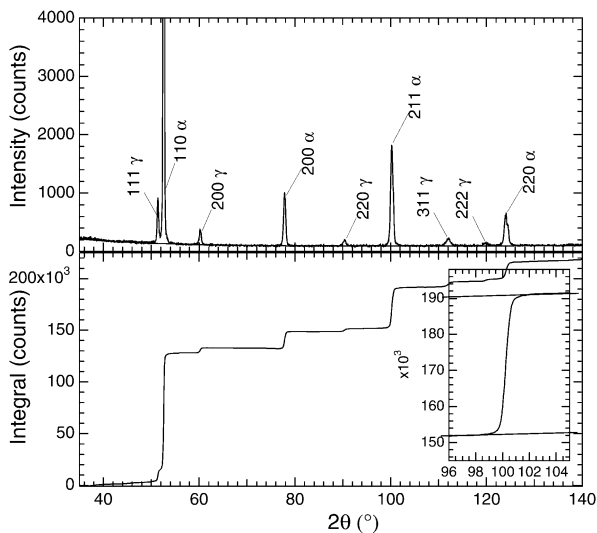


Fig. 1.27 Example of determining peak areas by background stripping and integrating. The method works the same way for peaks in diffraction patterns and in EDS energy spectra. *Top:* X-ray diffraction pattern from “Fe–9Ni Steel,” annealed at 600 °C to form austenite (fcc γ -phase) in tempered martensite (bct α' -phase) matrix, and subsequently quenched to 77 K to transform some of the γ -phase to α' -phase. An approximate background, modeled as a line function plus a decaying exponential, is fit to the data. *Bottom:* The model background was subtracted from the data, and the peaks were integrated, giving the indefinite integral in the graph. If the background model were perfect, the integral would have zero slope between the positions of the peaks. To accommodate errors in the background, the enlargement of the 211 α' peak (*inset at bottom*) shows *two parallel lines* of equal slope which were fit to the background region. The *vertical separation* between these lines, 38,350 counts, is the integrated area of the 211 α' peak

fraction, f_γ :

$$f_\gamma = \frac{0.65(I_{311\gamma} + I_{200\gamma})}{I_{211\alpha} + 0.65(I_{331\gamma} + I_{220\gamma})}, \quad (1.63)$$

where the notation $I_{331\gamma}$ denotes the integrated area of the 311 γ peak, for example. Equation (1.63) can be justified through (1.56), although the factor of 0.65 has been the subject of fine tuning by a number of workers.

The integrated areas of the peaks from the austenite and martensite phases are obtained numerically, as shown in Fig. 1.27. The integration procedure first requires an estimate of the background beneath the peaks, which is then subtracted from the diffraction pattern. The diffraction pattern is then integrated, and sharp jumps in the integral occur at the positions of the diffraction peaks. The areas of the peaks equal the size of these jumps if the background was determined accurately. Errors in the estimate of the background affect the area of the peak, but by assuming the residual error in the background is a constant, the procedure in the inset of Fig. 1.27 can be used to correct for it. The integrated areas of 311 γ , 211 α' , 220 γ peaks were deter-

mined to be 2,530, 38,350, and 4,260 counts, respectively. Using (1.63), a volume fraction $f_\gamma = 0.103$ is obtained.

1.5.13 Lattice Parameter Measurement

With a powder diffractometer it is possible to measure lattice parameters to an accuracy of better than 1 part in 10,000. This accuracy cannot be achieved, however, by simply applying Bragg's law to one peak in a diffraction pattern, owing to several practical problems. The most serious is that the center of diffraction is not located precisely at the center of the goniometer. This is caused by inaccurate sample positioning, irregularities of the specimen surface, and, more subtly, by variations in the x-ray penetration depth for different materials. The problem is illustrated in Fig. 1.28, where the misplaced specimen plane is indicated with a solid line.

The specimen displacement of Fig. 1.28 causes the measured diffraction peaks to shift to higher angles, θ . The shift in detector (and tube) position is $\varepsilon \cos \theta$, which gives an apparent error in diffraction angle, $\Delta\theta$:

$$\Delta\theta = \frac{\varepsilon \cos \theta}{R}, \quad (1.64)$$

where R is the radius of the goniometer circle. The effect on the lattice parameter is obtained by differentiating Bragg's law, where d_m and θ_m are the measured interplanar spacing and diffraction angle obtained with the shifted specimen:

$$\frac{d}{d\varepsilon} 2d_m \sin \theta_m = \frac{d}{d\varepsilon} \lambda, \quad (1.65)$$

$$2 \frac{dd_m}{d\varepsilon} \sin \theta_m + 2d_m \cos \theta_m \frac{d\theta_m}{d\varepsilon} = 0, \quad (1.66)$$

$$\Delta d_m \sin \theta_m = -d_m \cos \theta_m \Delta \theta_m. \quad (1.67)$$

Substituting (1.64) into (1.67),

$$\frac{\Delta d_m}{d_m} = \frac{\varepsilon \cos^2 \theta}{R \sin \theta}. \quad (1.68)$$

With a typical specimen shift of 0.25 mm and a radius of the goniometer circle of 250 mm, the fractional error in interplanar spacing, and hence lattice parameter, is typically 1 part in 1,000. Fortunately, for crystals with cubic symmetry we can correct accurately for this problem by examining the systematic trend of the lattice parameters obtained from a series of different Bragg peaks. We first obtain a lattice parameter, $a_0(\theta_{hkl})$, from the Bragg angle for each (hkl) diffraction peak:

$$a_0(\theta_{hkl}) = \frac{\lambda \sqrt{h^2 + k^2 + l^2}}{2 \sin \theta_{hkl}}. \quad (1.69)$$

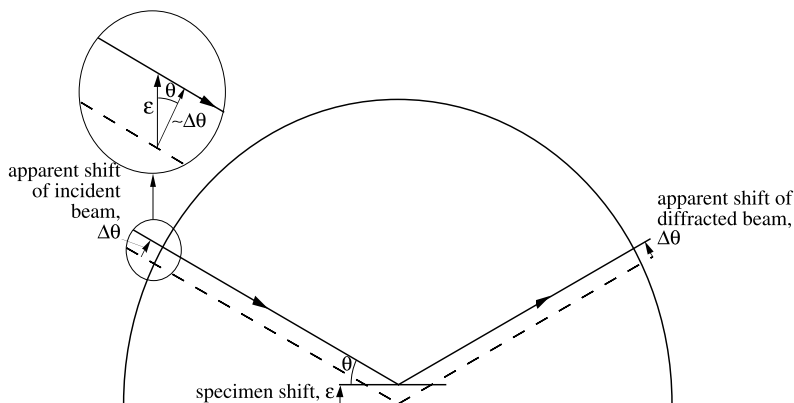


Fig. 1.28 Effect of sample displacement, ε , on apparent angles of diffraction

We then plot these values of $a_0(\theta_{hkl})$ versus the function $\cos^2 \theta / \sin \theta$ from (1.68). When we extrapolate this graph of $a_0(\theta)$ to the y-intercept where $\cos^2 \theta / \sin \theta = 0$, we eliminate the errors of specimen shift and x-ray penetration depth. (The extrapolated point corresponds to $\theta = 90^\circ$. From Fig. 1.28 we can see that Bragg peaks from the highest diffraction angles are affected least by ε .)

An experimental study of diffractometer errors was performed by Nelson and Riley [1.7], who suggested a slightly different extrapolation procedure. Instead of extrapolating the lattice parameter versus $\cos^2 \theta / \sin \theta$ of (1.68), the method of Nelson and Riley uses the empirical relationship:

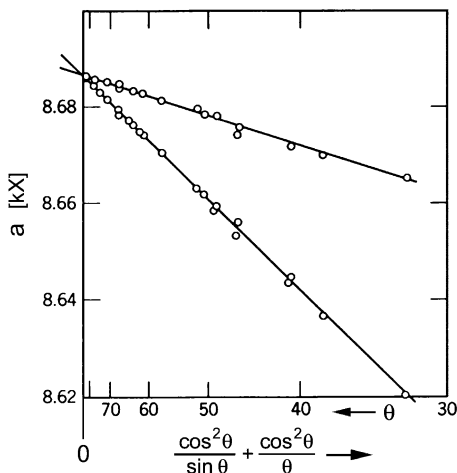
$$\frac{\Delta a_0}{a_0} \propto \frac{\cos^2 \theta}{\sin \theta} + \frac{\cos^2 \theta}{\theta}, \quad (1.70)$$

Figure 1.29 shows Nelson–Riley plots for two samples that differed in thickness, and hence in their effective centers of diffraction. Notice that the two extrapolations give nearly the same value of lattice parameter. The lattice parameter obtained from this plot is about 8.686 in the obsolete kX units, which can be converted to Angstroms by multiplying by the factor 1.002056.

1.5.14 * *Refinement Methods for Powder Diffraction Data*

The increasing power of computers, and their natural application for manipulating digital data, have led to a family of data analysis methods for powder diffraction patterns known as “refinement” methods (or “Rietveld refinement,” in honor of its pioneer, who distributed freely his method and code). The idea is to represent the experimental diffraction pattern, both peaks and background, with a multi-parameter mathematical model. The best set of these parameters is then found by an iterative calculation procedure that minimizes the difference between the calculated and

Fig. 1.29 Nelson–Riley extrapolations for two specimens of filings of $\text{Cu}_9\text{Al}_{14}$. After [1.8]



measured diffraction patterns. The typical criterion for goodness-of-fit is the minimization of a number, R (proportional to χ^2 of a statistical test):

$$R = \sum_{i=0}^M \frac{1}{\sqrt{N_i^{\text{ex}}}} [N_i^{\text{ex}} - N_i^{\text{c}}]^2, \quad (1.71)$$

where M is the number of data channels in the diffraction pattern (or at least those data points encompassing the diffraction peaks), and N_i^{ex} and N_i^{c} are the number of counts in the experimental and calculated data point i . The statistical error of each data point is assumed proportional to $\sqrt{N_i^{\text{ex}}}$, as is the case for ideal counting statistics. The calculated diffraction pattern, $\{N_i^{\text{c}}\}$, is determined by parameters that are adjusted iteratively, or “refined,” to minimize R .

A wide variety of parameters can be refined, including lattice parameters, crystallographic site occupancies, and sample positioning error. The crystal structure itself is not practical for a refinement calculation, and must be provided as input information for the refinement code. On the other hand, the lengths of the crystal axes, such as the a - and c -axes of a hexagonal crystal structure, are almost always refined. It is also common practice to refine the shapes of the diffraction peaks. The variations of the peak shapes with diffraction angle, 2θ , can be used to determine structural features in the sample such as strain distributions and particle sizes.

Rietveld refinement methods utilize the entire diffraction pattern of a crystal structure. This is superior to an analysis of only one or two peaks in the diffraction pattern for obtaining certain types of information about the sample. For example, for phase fraction measurements on samples that contain multiple crystal structures, a refinement analysis is less sensitive to problems of overlaps of diffraction peaks. More information is contained in a full diffraction pattern than in individual peaks.

This is especially true for structural features that have a characteristic dependence on diffraction angle, 2θ , (or diffraction vector, $\Delta\mathbf{k}$). The mathematical model in the refinement calculation accounts automatically for Δk -dependencies from the Lorentz-polarization factor and the atomic form factor (described in Chap. 4). Any residual Δk -dependence can then be attributed to atomic disorder or thermal displacements, for example.

Rietveld refinement methods were developed originally for the analysis of neutron powder diffraction patterns, where the shapes of diffraction peaks tend to be reproducible, and often have a simple mathematical form such as a Gaussian function. Peak shapes for an x-ray diffractometer, as discussed in Sect. 9.1, are not expressed easily as a simple mathematical function. Some sort of expression for peak shape is required, of course, since the underlying mathematical model must be fit to experimental data. Present refinement codes use a variety of functions, including a simple “pseudo-Voigt” function (the sum of a Gaussian and a Lorentzian function):

$$PV(x) = \eta L(x) + (1 - \eta)G(x), \quad (1.72)$$

where $0 < \eta < 1$, and the Gaussian and Lorentzian functions are given in (9.23) and (9.25). Another common function for x-ray peak shapes is the “Pearson VII” function, which has the canonical form:

$$P_{VII}(x) = \frac{1}{[1 + (2^{1/m} - 1)x^2]^m}, \quad (1.73)$$

where $x = (2\theta - 2\theta_0)/\Delta$, with $2\theta_0$ the peak center and Δ the peak width. Although the Pearson VII function is not obtained from a rigorous physical argument, by varying m from 1 to ∞ this function is capable of being a Lorentzian function or approximating a Gaussian function. Experimentation with peak shape is usually required. The choice of peak profile functions can affect the success of refinement calculations—it is important that discrepancies in peak shape do not make a significant contribution to the RMS error of the calculated diffraction pattern. Unfortunately, peak shapes do vary between samples, owing to effects such as absorption and multiple scattering. It is hoped that future versions of refinement codes will employ “learned peak shape functions,” which would be obtained by running a set of known standards in the diffractometer.

Refinement calculations begin with initial guesses at the background, peak width, and unit cell parameters of a crystal structure. It is usually impossible to perform a refinement calculation from start to finish by making just one guess at the initial parameters, however. Parameters are usually refined sequentially, with the most important ones first. Different refinement sequences are required by different software packages, but it is typical to first perform a refinement of background and the scale factors for the intensities of the diffraction patterns. The next steps typically involve refining the lattice parameters and the sample positioning error (Sect. 1.5.13). The peak shape is then refined further. Depending on the differences in atomic form factors, the site occupancy parameters may be important to refine earlier or later in the sequence, but for either case it is usually necessary to consider the heavy atoms first.

The temperature factor is typically refined later in the sequence, and the temperature factors for the individual atoms are often refined quite late in the sequence and may not be reliable. Some of the refined parameters, especially those obtained in the later parts of the sequence, may be sensitive to details of the sample preparation. The surface of the sample may not be flat, and this may cause, for example, inaccuracies in the absorption correction and unphysical thermal parameters.

Throughout the sequence it is usually necessary to inspect visually the progress of the calculated diffraction pattern. The residual, or the difference between the calculated and experimental diffraction pattern (ideally a line of zeroes), is especially useful for this purpose. Besides showing if the calculation is diverging or settling into a false minimum, visual inspection is useful for identifying the presence of second phases, which may have been missed in an initial inspection of the experimental data.

Many types of conditions can be imposed on refinement calculations. For example, it may be helpful to impose hard geometrical constraints, such as preventing two large atoms from approaching below a minimum distance. Soft constraints, implemented for example as penalty functions added to R (on the right-hand side of (1.71)), can be used for guiding the convergence of the refinement. The user of the refinement software may also consider modifying the refinement code for his or her own needs. For example, the present codes are not flexible for modeling crystallographic texture of a polycrystalline sample, but texture can alter significantly the relative intensities of diffraction peaks. If the experimenter has some knowledge of the crystallographic texture in the sample, it may be useful to impose this texture upon the mathematical model, either as a fixed ratio for the diffraction peaks or as a refineable parameter(s).

1.6 Further Reading

The contents of the following are described in the Bibliography.

L.V. Azároff, *Elements of X-Ray Crystallography* (McGraw-Hill, New York, 1968), reprinted by TechBooks, Fairfax, VA

B.D. Cullity, *Elements of X-Ray Diffraction* (Addison-Wesley, Reading, MA, 1978)

International Tables for X-ray Crystallography (Kynock Press, Birmingham, England, 1952)

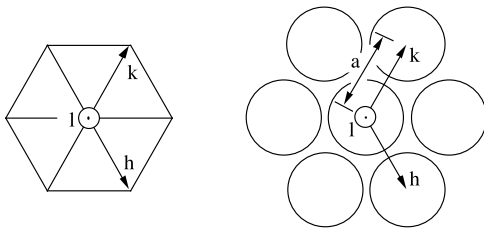
H.P. Klug, L.E. Alexander, *X-Ray Diffraction Procedures* (Wiley-Interscience, New York, 1974)

L.H. Schwartz, J.B. Cohen, *Diffraction from Materials* (Springer-Verlag, Berlin, 1987)

B.E. Warren, *X-Ray Diffraction* (Dover, Mineola, New York, 1990)

Crystal structure determination by single crystal x-ray diffraction methods is a large topic, and much of it is beyond the scope of the present book. This subject is covered in books by M.F.C. Ladd, R.A. Palmer, *Structure Determination by X-ray Crystallography* (Plenum Press, New York, NY, 1993), and G.H. Stout, L.H. Jensen, *X-ray Structure Determination: A Practical Guide* (Wiley-Interscience, New York, NY, 1989)

Fig. 1.30 Basal plane of hcp structure. The c -axis points up



1.7 Problems

1.1 Here are some features of powder diffraction patterns from a hexagonal close-packed crystal structure. We use a 3-index notation for the crystal planes, $(hk \cdot l)$, where the vector directions associated with the indices h and k point along columns of atoms oriented 120° with respect to each other in the basal plane. The vector direction associated with the l -index is perpendicular to the basal plane. These unit vector directions are shown in Fig. 1.30. The interplanar spacings, $d_{hk \cdot l}$, of a hexagonal close packed crystal are related to the nearest neighbor distance, a , as:

$$d_{hk \cdot l} = \frac{a}{\sqrt{\frac{4}{3}(h^2 + hk + k^2) + (l/1.63)^2}}. \quad (1.74)$$

Here a denotes the distance between adjacent atoms along the h - and k -axes, and c denotes the distance between atoms along the l -axis. The c/a ratio of an ideal hcp crystal is 1.63. The structure factor rule for the hcp lattice states that diffractions vanish when:

$$\{l \text{ is odd}\} \text{ AND } \{(h + 2k = 3n) \text{ OR } (2h + k = 3n)\}.$$

Find the first six non-vanishing diffractions for the hcp lattice, and plot them versus the inverse of $d_{hk \cdot l}$. Compare your result to the positions of the lines in the Appendix A.1.

1.2 For high-energy electron diffraction in a TEM, another estimate of the precision of diffraction angles can be provided by the uncertainty principle:

$$\Delta p \Delta x \simeq \hbar. \quad (1.75)$$

We do not know the specific plane that scatters the electron, so Δx is set by the number of diffracting planes, N , times the interplanar spacing, d :

$$\Delta x = Nd. \quad (1.76)$$

The diffracted wave undergoes a change in momentum during scattering. Our Δp is the uncertainty in this momentum change. We phrase the problem as: “With an uncertainty in which plane is doing the scattering, what is the uncertainty in the change of momentum of the diffracted electron?”

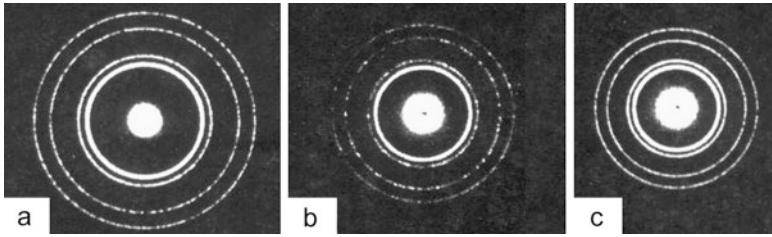


Fig. 1.31 Electron diffraction patterns from electrons with energies (a) 60 keV, (b) 80 keV, and (c) 100 keV [G. Thomas, M.J. Goringe, *Transmission Electron Microscopy of Materials* (Wiley-Interscience, New York, 1979)]. Reprinted by permission of John Wiley & Sons, Inc.

Using the de Broglie relationship, $p = h/\lambda$, show that small errors in wavelength, and hence the spread of diffraction angle, scale inversely with N .

1.3 This questions refers to the three electron diffraction patterns from a polycrystalline element shown in Fig. 1.31.

(a) Determine if the pattern is best indexed as an fcc pattern or a bcc pattern, and index the rings. You must use the structure factor rules of Sect. 6.3.2:

for fcc crystals h, k, l must be all even or all odd,

for bcc crystals the sum $h + k + l$ must be an even integer.

(b) Estimate a lower bound for the crystallite size by examining the widths of the rings. Assume the lattice parameter is 4.078×10^{-10} m.

1.4 Compare the θ -dependences of strain broadening and size effect broadening. For a fair comparison, we first linearize (1.7) (good for small θ) so that:

$$\Delta\theta_{\text{strain}} = -\varepsilon\theta_{\text{B}}. \quad (1.77)$$

The size effect broadening from (1.13) is, for $N \gg 1$:

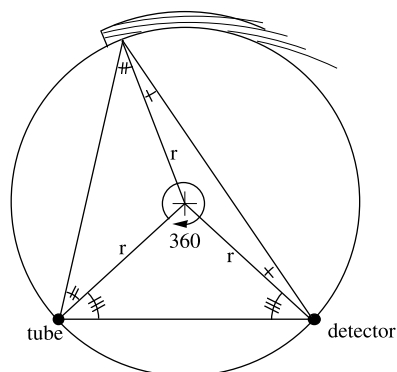
$$\Delta\theta_{\text{size}} = 0.9 \frac{\theta_{\text{B}}}{N}. \quad (1.78)$$

In a first glance at (1.77) and (1.78), it may seem that both the size and strain broadenings increase with the Bragg angle of the diffraction. This is in fact true for the strain broadening, but it is not true for the size broadening. Why?

1.5 Consider a polycrystalline sample of infinite thickness. As usual, the incident and diffracted rays both make the angle θ with respect to the plane of the sample surface. Absorption attenuates the intensity of an x-ray beam as: $I(x) = I_0 e^{-\mu_Q x}$ along a path of length x . Given incident and diffracted beams of the same cross-section, A_0 , show that the average attenuation of the beams through the specimen are independent of the angle θ .

Fig. 1.32 Focusing circle of

Fig. 1.17



(Hint: You should calculate the depth average of the absorption. The path length, x' , to reach depth z is: $x' = z / \sin \theta$, and the area illuminated goes as $A_0 / \sin \theta$.)

1.6 Consider the two ray paths from tube to detector in Fig. 1.17.

(a) Prove that the sum of the angles of incidence and diffraction (the total angles at the specimen) are the same for both ray paths.

(b) For the curved crystal planes (of radius $2r$) that touch the focusing circle, prove that the angles of incidence and diffraction are the same for both paths.

(Hint: Make use of isosceles triangles constructed with radii of the focusing circle as shown in Fig. 1.32.)

1.7 (a) Show that (1.26) for $\psi_{1s}(r)$ is an acceptable solution to the Schrödinger equation for the hydrogen atom. For normalization, multiply (1.26) by $(\pi)^{-1/2} (Z/a_0)^{3/2}$.

(b) Show that E for a $1s$ electron is equal to 1 Rydberg when $Z = 1$.

1.8 Explain why accurate measurements of lattice parameters are best performed using diffractions with large 2θ angles.

1.9 A large background in an x-ray diffraction pattern can be seriously detrimental to the data quality. This is a common problem for weak or diffuse diffraction peaks. In Fig. 1.33, notice how increasing the background from 0 to 100 to 400 counts affects the clarity of the peak centered at channel 63, which is of equal strength and shape in all three cases.

It is a result of probability theory that the statistical scatter of each data channel increases as \sqrt{N} , where N is the number of counts in that data channel. With a high background, the scatter in the data is dominated by the background count rate.

Show that when the peak-to-background ratio is small, for the signal-to-noise ratio (i.e., ratio of peak height to scatter at the peak):

Fig. 1.33 Three identical peaks on different noise backgrounds

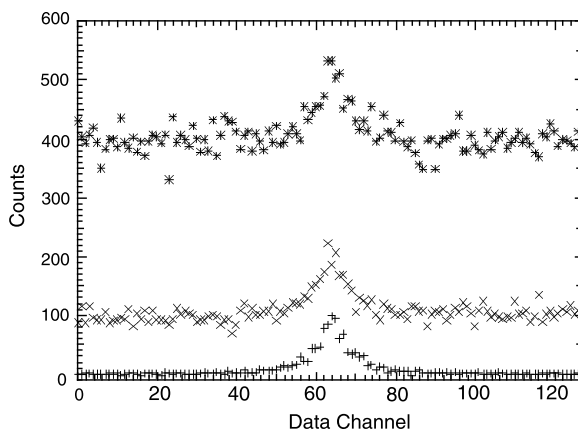
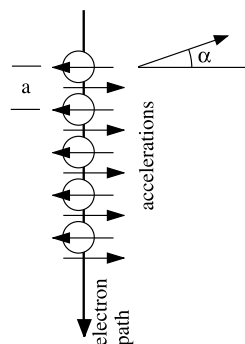


Fig. 1.34 Path of high-energy electron through atoms, and directions of its accelerations



(a) Halving the background countrate, while keeping the same countrate in the peak, is equivalent to increasing the counting time by a factor of 2.

(b) Doubling the strength of the peak (doubling its countrate) is equivalent to increasing the counting time by a factor of 4.

(c) How do your answers to (a) and (b) change when the peak is much stronger than the background (as in the lower data set of Fig. 1.33 with zero background)?

1.10 A phenomenon called “coherent bremsstrahlung” occurs when high-energy electrons travel through a periodic array of atoms as shown in Fig. 1.34. The high-energy electron travels in and out of the ion cores of the atoms, so it sees an electrostatic potential energy that oscillates with the period of the interatomic separation. The ensuing accelerations of the high-energy electron can cause radiation. In coherent bremsstrahlung, the wavelets emitted from each encounter with an ion core have phases that add constructively. Suppose the incident electron of velocity, v , travels along a column of atoms separated by a distance, a , labeled in Fig. 1.34.

- (a) What is the energy of the x-ray emission (nearly) perpendicular to the path of the electron? Express your answer using the result of (1.16).
- (b) For x-ray emission at angles, α , above or below the plane of the perpendicular, will the energy of the coherent bremsstrahlung be higher or lower than that of part (a)?
- (c) Calculate the energy dependence of the coherent bremsstrahlung on α .
- (d) Compare this emission of coherent bremsstrahlung to the emission of x-rays from an undulator inserted into an electron storage ring. In particular, why are the magnetic poles of the undulator spaced by cm dimensions, whereas the periodicity of Fig. 1.34 is in Å?

1.11 A problem occurs in x-ray diffractometry when the amplitude of a detector pulse decreases with countrate. At high countrates, the pulse amplitudes may fall below the setting of the lower threshold of the SCA. This problem distorts diffraction peaks in a similar way as detector dead time and the creation of sum peaks, which also become issues at high countrates. Answering qualitatively, how will these problems affect the peak shapes measured in an x-ray diffraction pattern?

1.12 Demonstrate the electric dipole selection rule for s and p electron wavefunctions. The electric dipole operator is $e\mathbf{r}$. The intensity of the transition $2s \rightarrow 1s$, for example, is proportional to the square of the integral

$$\langle 1s | e\mathbf{r} | 2s \rangle = \int_{-\infty}^{\infty} \int_{-\infty}^{\infty} \int_{-\infty}^{\infty} \psi_{1s}^* e\mathbf{r} \psi_{2s} dx dy dz. \quad (1.79)$$

- (a) Calculate $\langle 1s | e\mathbf{r} | 2s \rangle$ and show it is zero.
- (b) Calculate $\langle 1s | e\mathbf{r} | 2p \rangle$ and show it can be non-zero.

(Hint: For part (b), normalization is not important. It is simplest to use 1 for the s -wavefunctions, either x , y , or z for the p -wavefunctions, and align \mathbf{r} along either x , y , or z . Try all orientations of \mathbf{r} for part (b). Finally, you can ignore the divergence that is suppressed when the radial decays of the wavefunctions, ψ , are included.)

1.13 Draw an isosceles triangle with the wavevectors \mathbf{k}_i and \mathbf{k}_f separated by the angle ϕ (analogous to Fig. 6.22).

- (a) Instead of using the geometrical solution of Fig. 6.22, use the law of cosines ($c^2 = a^2 + b^2 - 2ab \cos \phi$, where $a = k_i$, etc.) to obtain Δk in terms of the Bragg angle, θ .
- (b) Draw the orientation of the Bragg planes on your figure, and draw their normal vector $\hat{\mathbf{n}}$. What is the angle between $\hat{\mathbf{n}}$ and $\Delta \mathbf{k}$?

Transmission Electron Microscopy and Diffractometry of
Materials

Fultz, B.; Howe, J.M.

2013, XX, 764 p., Hardcover

ISBN: 978-3-642-29760-1